Université de Montréal

Décharge électrique à l'interface de deux liquides : application à la synthèse de nanoparticules

Par

Kyana Mohammadi

Département de physique, Études supérieures et postdoctorales

Mémoire présenté en vue de l'obtention du grade de Maître ès Sciences (M. Sc.)

En Physique

September 2021

Université de Montréal

Département de Physique, Études supérieures et postdoctorales

---

Ce mémoire (ou cette thèse) intitulé(e)

Décharge électrique à l'interface de deux liquides : application à la synthèse de nanoparticules

Présenté par

Kyana Mohamamdi

A été évalué(e) par un jury composé des personnes suivantes

Luc Stafford
Président-rapporteur

Ahmad Hamdan
Directeur de recherche

Nick Virgilio
Membre du jury

Résumé

Les procédés plasma-liquide sont considérablement étudiés en raison de leur potentiel élevé dans la production de divers nanomatériaux, parmi d'autres applications technologiques. En plus d'un rendement relativement élevé (mg/min) et d'une infrastructure simplifiée, les mécanismes de synthèse sont directs. Le fait que les produits restent confinés dans la solution, la manipulation de nanomatériaux ne présente un danger ni aux vivants ni à l'environnement.

Dans ce mémoire de maitrise, les méthodes les plus courantes pour la synthèse de nanomatériaux, en particulier les systèmes plasma-liquide, sont discutées. La formation de différents régimes de plasma dans des liquides, dont chacun a des caractéristiques et des applications différentes, est présentée. Ensuite, le système multi-liquide et ses caractéristiques, telles que les caractéristiques électriques et la dynamique de l'émission des décharges dans différentes conditions, sont exposés.

Pour la synthèse de nanoparticules, on traite les décharges Sparks (étincelles) avec une attention particulière. Au lieu de les produire entre deux électrodes immergées dans un liquide diélectrique, les décharges sont produites dans un hydrocarbure liquide entre une électrode et une solution conductrice. Cette dernière est produite via l'ajout de nitrate d'argent dans l'eau. Le plasma, via ses espèces réactives, réduit les ions Ag^+ en Ag^0 qui forment ensuite les nanoparticules. La décomposition de l'hydrocarbure produit aussi des espèces carbonées qui se recombinent sous forme d'une matrice hydrocarbonée. En se basant sur différentes méthodes de caractérisations (FTIR, MEB, MET, UV-vis, etc.), nous identifions deux zones de réactions : dans le plasma dans l'heptane et à l'interface plasma-solution. Les produits dans la première zone sont majoritairement des nanoparticules (< 10 nm) d'Ag enrobées dans une matrice de carbone hydrogénée. Cependant, les produits dans la solution sont des nanoparticules d'Ag (sans matrice) ayant une distribution de taille de quelques dizaines de nanomètres.

Mots-clés : Plasma dans le liquide, décharge par étincelle, nanocomposite, décharges nanosecondes, nanoparticule d'argent, réseau d'hydrocarbures

Abstract

Plasma-liquid systems are significantly investigated due to their high potential in the production of various nanomaterials, among other technological applications. In addition to relatively high efficiency in production (mg/min) and simplified infrastructure, the mechanisms of synthesis are rather direct. Also, because the products are confined in solution, the handling of the nanomaterials do not present risks to the living or to the environment.

In this master thesis, the most common methods for nanomaterial synthesis, in particular plasma-liquid systems, are discussed. Formation of different plasma regimes in liquids, which each of them has different features and application, are explained. Then, the multiple liquid system and their feature such as electrical characteristics and emission dynamic of the discharges at different conditions, are investigated.

To produce nanoparticles, we present the Spark discharges with special attention. Instead of their production between two electrodes immersed in a liquid dielectric, the discharges are produced in a liquid hydrocarbon between one electrode and a conductive solution. This latter is prepared by adding silver nitrate to water. The plasma, through its reactive species, reduces the ions Ag^+ to Ag^0 that produces nanoparticles. The decomposition of the hydrocarbon produces carbonaceous species that recombine as hydrocarbon matrix. Based on the different characterisation techniques (FTIR, SEM. TEM. UV-vis, etc.), we identified two zones of reactions: in plasma in heptane and at the interface plasma-solution. The products in the former zone are majority 10 nm-particles of Ag embedded in a hydrocarbon matrix, while the products in solution are Ag nanoparticles (without matrix) with size of several tens of nanometers.

Keyword: Plasma in-liquid, spark discharge, nanocomposites, nanosecond discharges, silver nanoparticle, hydrocarbon network

Table des matières

Liste des tableaux

Liste des figures

In summary, this chapter described a novel plasma-liquid configuration, that is plasma in two immiscible liquids. The position of the electrode pin regarding the interface plays a major role on the plasma dynamics, as the interface strongly influences the electric field distribution. The conductivity of a solution has also a major role on the discharge mode, as it allows transition from streamer (at low conductivity) to spark (at high conductivity). In the next chapter, we will focus

Liste des sigles et abréviations

This thesis is dedicated to my parents. For their endless love, support and encouragement.

Remerciements

I would thank my parents from the bottom of my heart, although for them my heart has no bottom. Thanks to my brother for all support and for encouraging me to go further.

I would like to thank Professor Ahmad Hamdan, my supervisor, who has always guided and supported me during these two years in every step. Without his help, I could have not finished my paper and my thesis manuscript.

Also, I would like to thank the jury members, Prof. Luc Stafford (Université de Montréal) and Prof Nick Virgilio (Polytechnique Montréal) for their time, efforts, and guidance to enhance the quality of the thesis.

Thanks to my colleague and friend Thomas Merciris, who helped me a lot with my experiments. And thanks to James Diamond and the whole research group.

Introduction

Nanoparticles are now used in a variety of fields, including medicine, food, and industrial processes for many applications such as biosensors [1], food preservatives [2], fuel cells [3], solar panels [4], and water purification [5]. Several physical, chemical, or biological methods of nanomaterial synthesis have been developed to date [6,7]; however, the synthesis of these nanoparticles safely and efficiently remains a challenge.

Plasma-based methods have recently demonstrated significant potential for use in the synthesis of nanomaterials [8,9]. For instance, the plasma torch is a well-known technique for fabricating a variety of nanomaterials, including titanium oxide [10] and carbon nanotubes, among others [11,12], via the processing of solid [13], liquid [14], or suspension [15] precursors. Another well-known technique is laser ablation, used in gaseous [16-18] and liquid environments [19,20]. Many materials can be processed using laser ablation such as aluminum [21] and zinc [22] among many others.

One of these plasma methods, which can be considered as a relatively new field of research, is the plasma-liquid. Plasma-liquid based methods have demonstrated high efficiency (mg/min) in addition to be environmentally friendly (no additives are required) in the production of nanomaterials [23]. The high efficiency is due to the reactive nature of the plasma (which is an ionized gas containing a rich source of energetic species, reducing and oxidizing specious, radicals, etc.) and to the high density of liquid. Thus, various chemical and physical processes may occur at the plasma-liquid interface.

Plasma-liquid interactions can be produced in one of three ways: (i) in a gas phase in contact with the liquid [24-26], ii) directly in the liquid [23], or iii) in multiphase environments [27,28]. Each of these systems can be achieved in different configurations and features that are tailored to produce different nanomaterials and nanostructures like core-shell, nanocomposites, nanoalloys, etc.

In this thesis, we investigate the production of plasma in the presence of two liquids: one dielectric (hydrocarbon liquid) on top of a conductive solution. The dielectric liquid is n-heptane and the conductive solution is water + silver nitrate. In this configuration, a stable interface between the two liquids is established. A plasma discharge was sustained between an anode pin (made of carbon rod) in heptane and the solution surface (i.e. the interface); the cathode was immersed in solution far from the interface and is not interacting with the discharge. The discharge was characterized as spark, and two kinds of materials were produced: Ag nanoparticles embedded in a hydrocarbon network collected in heptane side, and Ag particles in solution. The produced particles were characterized using transmission electron microscopy (TEM), electron dispersive spectroscopy (EDS), ultraviolet-visible (UV–vis) absorption spectroscopy, and Fourier transform infrared (FTIR) spectroscopy. Furthermore, plasma properties in such system were investigated by optical emission spectroscopy and photomultiplier analysis. The effect of the plasma lifetime on produced nanoparticles are studied as well by adjusting the high voltage pulse width.

Chapter 1 –Literature review of plasmas for nanomaterial synthesis

1.1- Nanomaterials synthesis methods

Richard Feynman, an American physicist who won the Nobel Prize in 1965, coined the term "tiny systems" in 1959 during the annual American Physical Society conference [29]. In the early 1980s, approximately two decades after Feynman's speech, research into nanoscience and nanotechnology began, with the invention and development of various spectroscopic techniques such as scanning tunnelling microscopy (STM) in 1982 and atomic force microscopy (AFM) in 1986 [30]. In 1974, Norio Taniguchi introduced the term 'nanotechnology.' "Nanotechnology mainly consists of the processing, separation, consolidation, and deformation of materials by an atom or a molecule," [31,32].

The field of nanotechnology has rapidly grown in recent decades due to the fascinating physical, chemical, mechanical, and electrical properties of particles at the nanoscale [33-35]. Nanoparticles can be synthesized in a variety of compositions, sizes, shapes, and morphologies, allowing for their use in a range of applications, including catalysis [36], drug delivery [37], sensing [38], energy storage [39], and biomedicine [40] (Figure 1).

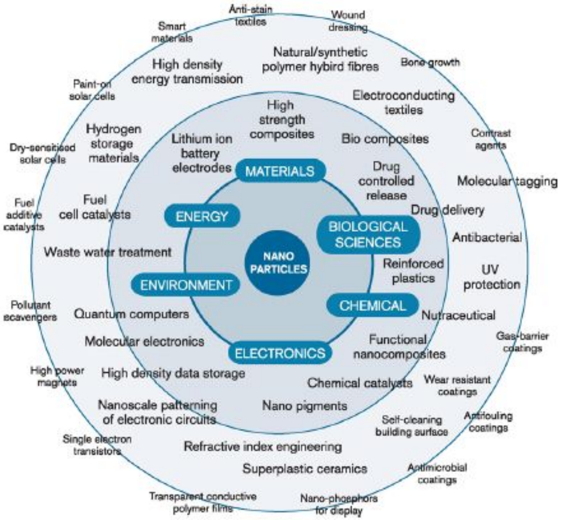

Figure 1. – Various applications that utilize nanoparticles [41]

Different approaches to nanomaterial synthesis are referred to as top-down and bottom-up methods (Figure 2). Top-down methods like mechanical milling, etching, and sputtering involve breaking down a bulk material into small particles to reach nanoscale materials. The bottom-up approach includes the assembly of atoms and molecules through processes such as hydrothermal [42], solvothermal, and chemical vapor deposition (CVD) [43].

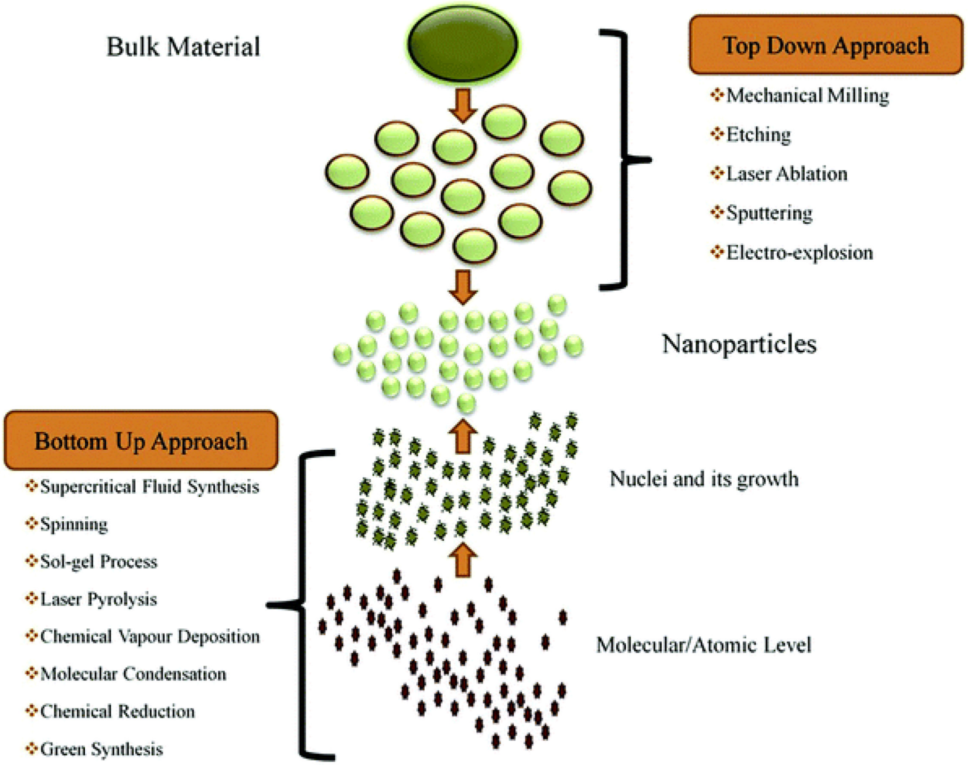

Figure 2. – Synthesis of nanomaterials (NPs) via top-down and bottom-up approaches [44]

Plasma-based synthesis methods have demonstrated significant potential for use in the bottom-up and top-down synthesis of nanomaterials. These techniques are expected to be used to synthesize advanced multifunctional nanomaterials and nanocomposites [45].

1.2- Plasma-based methods for nanomaterials synthesis

Sir William Crookes introduced plasma as a "radiant matter" in 1879 during his lecture to the British Association for the Advancement of Science, and Irving Langmuir proposed the term 'plasma' as the fourth state of matter in 1928. Plasma is formed when a gaseous medium is ionized [46]. It is composed of electrons, positive and negative ions, neutral particles, metastable species, excited atoms or molecules, and reactive radicals.

Plasmas are classified into two broad categories based on their temperature: high-temperature (hot) plasmas and low-temperature plasmas. In high-temperature plasmas, the gas is completely ionized, and the plasma is in thermodynamic equilibrium, which means that all plasma species (ions, atoms, and molecules) have the same high temperature. Low-temperature plasmas have significantly lower temperatures than high-temperature plasmas, and their degrees of ionization are typically much less than one. Species of low temperature plasmas have varying temperatures. For example, electrons have a temperature of approximately ~10^4 K, while heavy particles such as ions and neutral species have a temperature of only a few hundred K [47].

1.3- Common plasma methods for producing nanomaterials

Numerous plasma sources have been developed and applied in the nanomaterial's synthesis process. This section briefly discusses several gas-phase systems, including dielectric barrier discharges (DBD), plasma jets, and laser-based systems, before delving into plasma-liquid systems in greater detail.

1.3.1- DBD plasma

DBDs can be generated in many configurations, but the simplest is to use conductive electrodes, most commonly metals, and to cover one or both electrodes with a dielectric material such as glass, quartz, ceramics, mica plastics, or Teflon. The electrodes are connected to a high voltage source, and an electrical breakdown occurs in the gap between the electrodes, resulting in the formation of a plasma. Thus, the dielectric prevents the formation of an arc discharge and protects the material from excessive heat transfer and thermal damage [48]. The fundamental mechanisms underlying a DBD's operating modes (homogeneous or filamentary) are well documented in the literature [49]. Regarding its application in the synthesis of materials, a recent example is provided here.

Massines et al. used an argon atmospheric pressure dielectric barrier discharge to synthesized gold/polymer nanocomposite thin films (Figure 3). They injected an aerosol of a solution of gold salts dissolved in a polymerizable solvent (isopropanol) into a DBD, which resulted in plasma-ionized species reducing the metallic salt and energetic species polymerizing the solvent, resulting in thin films of metal-polymer nanocomposites on a large surface [50].

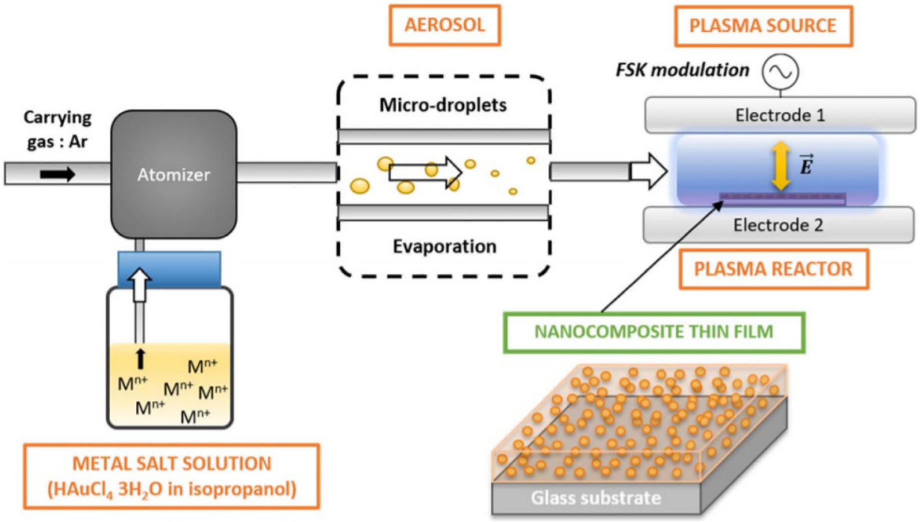

Figure 3. – Nanocomposite synthesis procedure [50]

1.3.2- Plasma jet

Another frequently utilized source is plasma jet, which is extensively used in the synthesis of nanomaterials. Plasma can be generated using radio frequency (RF), inductive or capacitive coupling, alternating current (AC), or pulsed power. Precursors can be transported through the tube or placed directly in contact with the plasma outside the tube. Figure 4 illustrates several setups of plasma jets to synthesize nanomaterials [52].

These systems can fabricate a broad range of metals, metal–oxides, and semiconductor nanostructures. For example, Kortshagen et al. produced single-crystal silicon nanoparticles with diameters ranging from 20 to 80 nm using a constricted, filamentary capacitively coupled low-pressure plasma [53].

Additionally, these methods can be used to form nanocomposites and novel nanostructures. For example, Cho et al. synthesized W-x wt% Cu (x= 5, 10, and 20 wt%) nanocomposites by injecting the blending micro powder of tungsten trioxide (WO_3) and cupric oxide into an inductively coupled radiofrequency (RF) thermal plasma (CuO). Furthermore, they created Ni-W nanostructures using a similar method. These nanostructures are a nonconventional alloy system, and they are an excellent electrode candidate for highly integrated microcircuit applications [54,55].

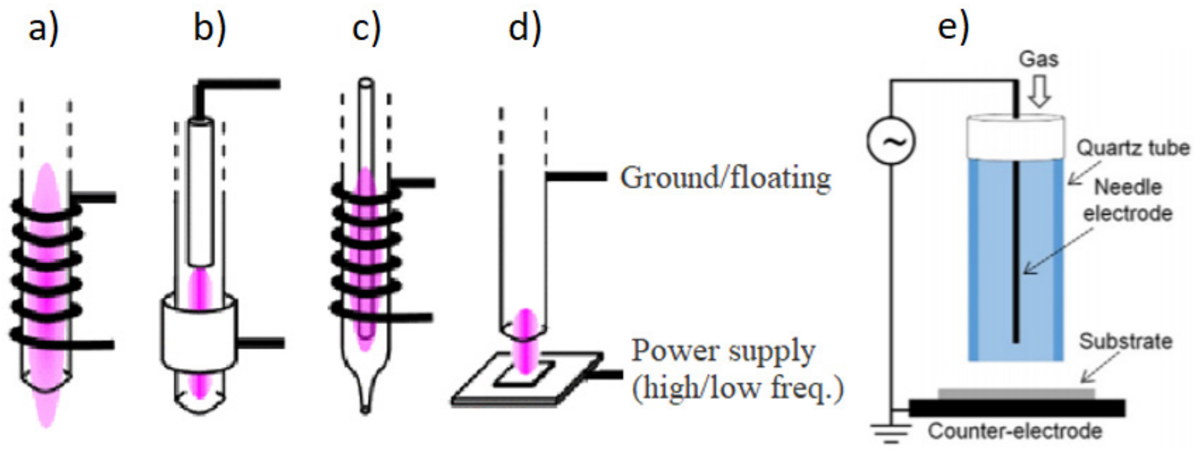

Figure 4. – Schematic diagram of the microplasma jets a,b,c,d) With external electrodes and e) With a consumable Au wire electrode [56].

Another type of plasma jet makes use of consumable precursors in the form of metal wire electrodes (inserted into the tube). The wire is heated and melted, and the evaporated matter in the plasma agglomerates to form nanomaterials. Shimizu et al. used this configuration to melt a 100 μm diameter Au wire contained in a capillary in the vicinity of an H_2/Ar mixture gas flow, resulting in the formation of Au nanoparticles [57].

1.3.3- Microwave plasma

Vallath et al. [58] demonstrated the first microwave plasma system to synthesize ceramic oxide powders. This system is comprised of a resonant microwave cavity connected to a waveguide, as illustrated in Figure 5a. The precursor is vaporized in Ar/O_2 stream (reaction gas) and flowing through the reaction tube. This tube passes the resonant microwave cavity, igniting a plasma at the microwave cavity's intersection with the reaction tube. Such a system was used to synthesize nanopowders of ZrO_2 (precursor of $ZrCl_4$), Al_20_3 (precursor of $AlCl_3$), and TiO_2 (precursor of $TiCl_4$) with diameters ranging from 5 to 30 nm [58].

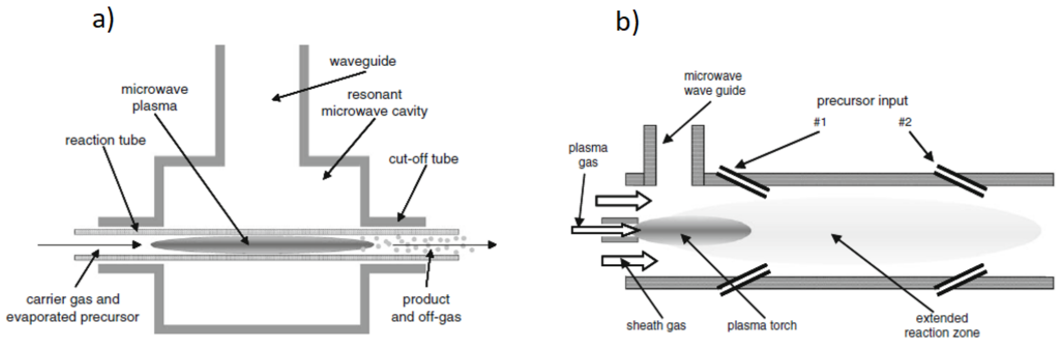

Figure 5. – Microwave plasma system working at a) Low pressure and b) Under ambient pressure [58,59].

Microwave plasma systems can operate at both low and high pressures. Small particles (5 to 30 nm) can be produced in low-pressure systems. However, a broad particle size distribution (up to 50 nm) is produced when operated at atmospheric pressure. Figure 5b depicts a schematic of a typical microwave plasma setup operating at atmospheric pressure. Precursors can be introduced into the microwave plasma torch at various locations in this system. As a result, because the temperature and species density may be varied, the properties of the particles produced can be adjusted [59].

1.3.4- Laser-induced plasma

Generally, laser-driven plasma processes used to manufacture nanomaterials can be classified as laser using gaseous targets or laser ablation processes through solid targets. The former involves focusing the laser above an aperture through which a mixture of precursor and gas flows. A laser beam is focused on that location to induce plasma and synthesis of nanomaterials (Figure 6a). The precursor and gas mixture are selected based on the desired nanomaterial. For example, using $Fe(CO)_5$ as a precursor and C_2H_2 as a carrier gas, David et al. produced α-Fe particles embedded in graphite [60]. Alexandrescu et al. synthesized two oxide semiconductors: gamma iron oxide (γ-Fe_2O_3) using laser-induced pyrolysis of a mixture containing iron pentacarbonyl/air/ethylene, and titania (TiO_2) semiconductor nanoparticles via the laser pyrolysis of $TiCl_4$- (vapors) based gas-phase mixtures. [61].

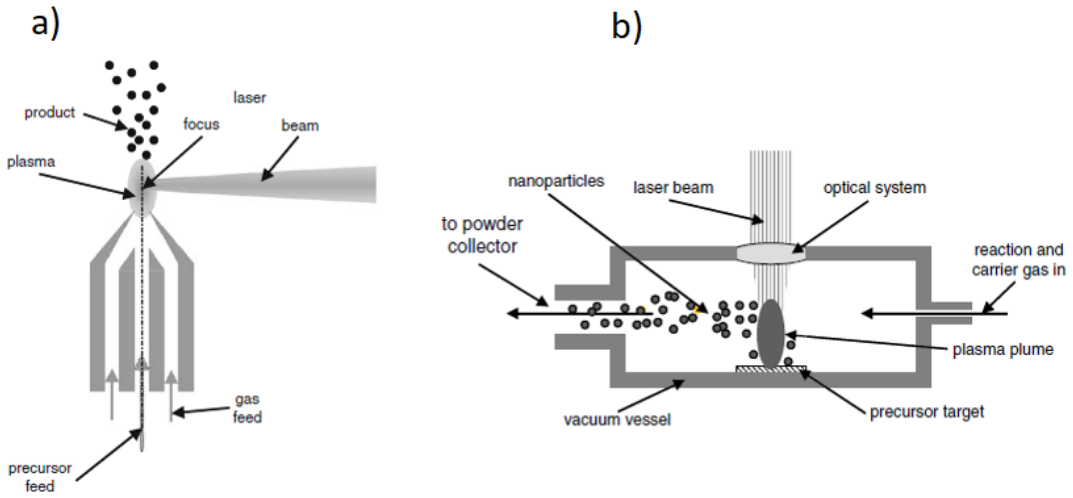

Figure 6. – Laser-driven plasma systems for nanoparticle synthesis a) With a gaseous target and b) A solid target [60,62]

Laser ablation of a solid target has been carried out in either a gaseous or liquid medium. Figure 6b illustrates a typical experimental arrangement for the former [62]. A pulsed laser beam is focused on the surface of a target, which can be a metallic, ceramic, oxide, or any complex mixture of these materials. As a result of the laser focus's high energy density, the target evaporates, and the plasma plume forms perpendicular to the target surface.

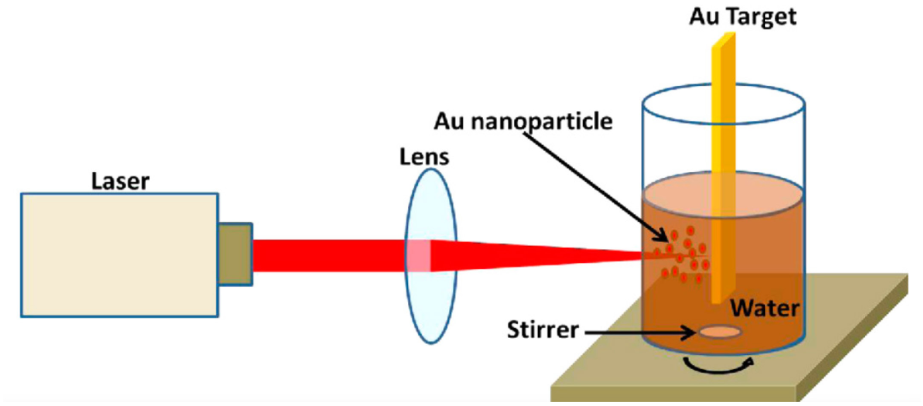

Figure 7. – Schematic depicting a laser ablating a gold target in water [63]

The schematic of the other case, laser ablation of solid target in liquid environment system, is shown in figure 7 [63]. Patil et al. reported the first application of pulsed laser ablation at the solid-liquid interface in 1987 when they created a metastable form of iron oxide from a pure iron target material [64].

Numerous liquids can produce a variety of different types of nanoparticles. For example, Bozon-Verduraz et al. synthesized Ti, Si, Ag, and Au nanoparticles via laser ablation of metal targets immersed in a liquid environment (H_2O, C_2H_5OH, $C_2H_4Cl_2$) [65], or Koshizaki produced TiO_2 nanocrystals under pulsed-laser ablation of a titanium target immersed in an aqueous solution of surfactant sodium dodecyl sulfate (SDS) and deionized water [66].

Furthermore, different liquids have varying effects on the production of nanoparticles. For instance, Musaev showed that laser ablation of a Tin (Sn) target in water results in polycrystalline tin dioxide (SnO_2) nanoparticles; however, ablation in ethanol results in single crystals of tin nanoparticles coated with tin hydroxide ($Sn(OH)_2$) [67].

1.4- Plasma-liquid systems

Until approximately 30 years ago, the field of plasma-liquid interactions was primarily concerned with glow discharge electrolysis and the breakdown of dielectric liquids for high voltage switching [68,69]. It can be said that this field has only addressed a variety of applications in the last 15 years, most notably the synthesis of nanomaterials. Three types of plasma-liquid systems exist:

- Plasma in liquid
- Plasma in gas in-contact with a liquid
- Plasma in multi-phase environment:
    - Plasma in bubbles in liquid
    - Plasma with liquid droplets
    - Plasma in an immiscible liquid.

1.4.1- Plasma in liquid

The most frequently used geometries for generating plasma in a liquid medium are pin-to-pin or pin-to-plate electrodes (Figure 8). Different discharge regimes, such as corona, streamers, spark, or arc, can be sustained depending on the experimental conditions.

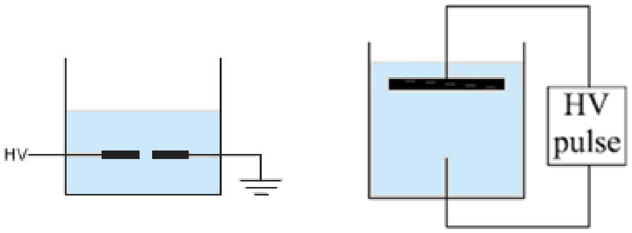

Figure 8. – Schematic of direct discharge in liquid

Corona discharge is a region of plasma formed around the electrode tip when a high voltage is applied, and the fluid around the tip is ionized. Generally, divergent electrode geometry, such as the pin-to-plate, is required to avoid spark breakdown of the inter-electrode gap when a high electric voltage is applied (Figure 9).

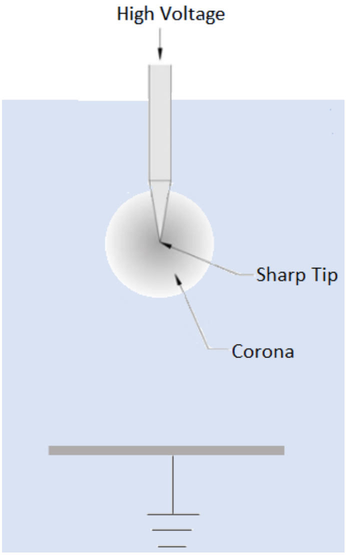

Figure 9. – Corona discharge in liquid

Ionization processes determine the corona onset voltage (Vs) at the electrode tip, and the applied high voltage must be more than this voltage (V > Vs) for discharge to occur. Due to the strong electric field near the electrode tip, the positive ions density increases exponentially in this region, distorting the electric field and resulting in a non-Laplacian field. The distorted electric field induces the formation of a thin layer called the cathode sheath, which contains intense ionization [70]. In this layer, the electric field and ionization generate a strong electronic current in this layer, maintaining a steady-state electric current inside the electrode gap. This mechanism is used to describe corona discharge in both gases and high-density environments such as liquid

Argon [71]. However, the corona in a liquid has some different features from the one in a gas. For instance, Bonifaci et al. demonstrated that the "cathode sheath" properties in a liquid (e.g., liquid helium) differ from those in a gas. The gaseous cathode sheath has similar properties to the positive column of a glow discharge in low-density gases [72], i.e. it contains a layer of quasi-neutral plasma with equal electron and positive ion densities and constant electric field strength. Nevertheless, because liquids experience a more significant impact ionization and have a shorter mean free path for electrons than gases, this neutral structure does not exist in liquids.

Before discussing the theory of the *streamer* or *arc* in liquid, the formation of these modes in the air will be discussed due to the mechanism's similarity. By increasing the voltage or employing nanosecond pulse discharge, the corona can be transient to the streamer, propagating toward the cathode electrode (positive streamer, Figure 10a) or toward the anode electrode (negative streamer, Figure 10b). Propagation of positive and negative streamers is influenced by two critical factors: 1) drift and diffusion of electrons; and 2) photoionization process [73]. If the plasma reaches the opposite electrode, a conductive channel bridges the gap between the electrodes, resulting in a spark (Figure 10d) or an arc (Figure 10e), depending on the power supply.

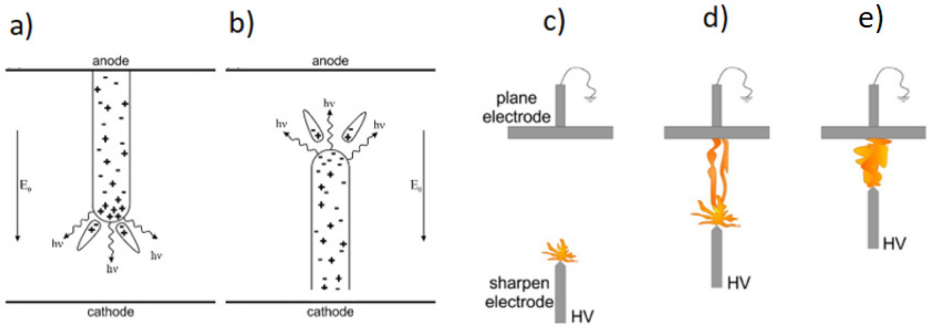

Figure 10. – Illustration of the propagation of a) Positive and b) Negative streamers, and c,d,e) Demonstration of different electrode gaps resulting in streamer, spark, and arc regimes, respectively [74].

The electrical characteristics of a discharge and the sequence of events that occur during the formation of a spark in a dielectric liquid are depicted in Figure 11 [75]. As previously stated, the discharge mechanism in liquids is more complicated than in other media such as gases due to the much higher density of molecules in liquids. Thus, the mechanism is dependent not only on phenomena occuring in gas discharge such as electronic collisions, but also on other phenomena such as molecule interactions.

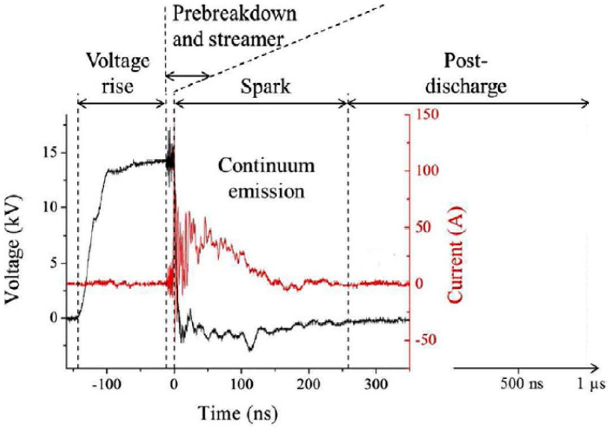

Figure 11. – electrical characteristics of a discharge formation in a dielectric liquid as a function of time [75].

Kuskova proposes a theory to describe plasma in liquid process [76]. The mechanism for plasma ignition in the gas phase is identical to this theory; the only difference is the species variety, i.e., plasma created by electron multiplication in the gas phase. It can, however, be generated by ions in the liquid phase. For example, during a nanosecond discharge in water, it dissociates into H^+ and OH^- in a high field area, such as an electrode pin, and forming a conductive region. The electric field of this conducting region forms a new conducting region, and like electron avalanches, this trend continues and propagates through the liquid as an ionization wave. This theory is almost always used to explain plasmas produced by nanosecond pulse voltage, because the energy is distributed solely to the electrons and not to the heating of the liquid [77].

If the discharge trigged by microsecond (or longer) pulses, bubble theory can be used to describe plasma formation [78]. According to this theory, microbubbles form near the electrodes due to the liquid being heated by field emission (Joule heating). When a critical value of the low-density region is obtained by these microbubbles, discharge, or electron avalanche resulted in liquid ionization and form conductive channels (streamers). If the electric field is applied long enough, the streamers can lengthen the gas channels and also form additional gas channels that propagate through the liquid or transit to the spark or arc.

There are also other hypotheses that define the formation of bubbles regarding to the sub-microsecond discharges by non-thermal process. According to these hypotheses, there is a possibility of crack propagation or micro-cavities in the liquids. The former is created by electrical stress, while the Lippmann effect forms the latter. This effect is the reduction of surface tension by rising electrical field. As a result of the enhanced electric field near the electrode, cavities form on the electrode [79,80]. Finally, after plasma is generated in a liquid, various reactive species such as $H^{\bullet}$, $OH^{\bullet}$, and radicals interact with the liquid medium and the electrode surface, resulting in the formation of numerous physical and chemical processes, leading to nanomaterial production, among other applications.

1.4.2- Plasma in gas in contact with a liquid

Gubkin conducted the first experiment involving plasma in contact with liquid in 1887, using a glow discharge between a metal anode and an aqueous solution ($AgNO_3$) as a cathode. He observed a layer of metal particles at the plasma-liquid interface formed due to plasma electrons reducing metal cations [81]. Plasma can be coupled to a liquid directly or indirectly. Direct coupling occurs when the liquid is considered an electrode (anode or cathode), which means the plasma is electrically connected to the liquid. However, due to the indirect coupling, plasma generation is independent of the liquid, even though the latter affects its properties [82].

1.4.2.1- Plasma directly coupled with liquid

Most of the studies were conducted in highly simplified geometric configurations: pin-to-liquid (Figure 12a). Except for ionic liquids, almost all these systems operate at atmospheric pressure or higher [83]. Depending on the experimental conditions (applied voltage, pin curvature, inter-electrode distance, and others), various discharge regimes have been reported, namely, corona, glow, or glow-to-spark transient.

Yang et al. used the system depicted in Figure 12b to synthesize carbon nanotubes (CNT) decorated with Au NPs [84], and Pd NPs in such a way that for Pd-MWNTs, the cathode is immersed in the liquid, and as the Ar gas passes through the system, the glow discharge plasma is generated between the anode (stainless steel) and the ionic liquid surface (1-butyl-3-methylimidazolium tetrafluoroborate plus MWNTs and $Pd(OAc)_2$ dispersed in ethanol) [85].

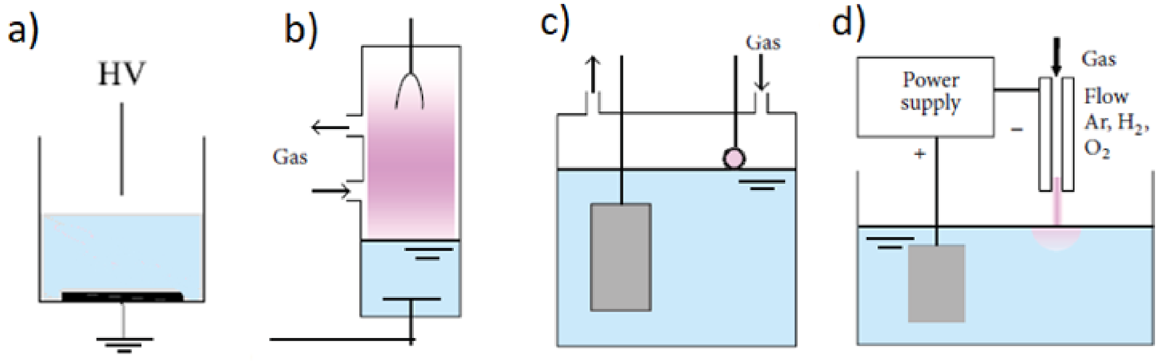

Figure 12. – Different configurations of plasma over liquid systems a) Pin to liquid b) Gas-liquid interfacial plasma [84], c) Discharge electrolysis [86] d) Microplasma over liquid [87]

The electrode in Figure 12c is in close contact with the electrolyte's surface, and when a high DC voltage is applied between the anode and cathode immersed in the electrolyte, a glow discharge occurs between the anode and the liquid surface. Kawamura et al. used plasma-induced cathodic discharge electrolysis in a molten chloride electrolyte to synthesize nanomaterials, including Ag, Si, SiC, Al, Zr, Fe, CoPt, Sm-Co, and FePt [88-92].

In Figure 12d, a metallic capillary tube is considered as the cathode; Ar or He gas is injected through the tube, resulting in the formation of microplasma. Richmonds et al. used this method to synthesize different metal nanoparticles such as Ag, Ni, Fe, and NiFe nanoparticles [24,93]. Additionally, Mariotti et al. reported Au and Si nanoparticles in this technique [94,95].

Plasma over liquid systems strongly interact with the liquid, and a significant portion of the discharge power is dissipated in the liquid, resulting in large evaporation rates when the liquid electrode serves as the cathode.

When the liquid acts as the cathode, there is a significant cathode fall at the liquid surface, whereas when the liquid acts as the anode, there is no voltage fall at the liquid surface, as illustrated in Figure 13 (Kaneko et al.) [96].

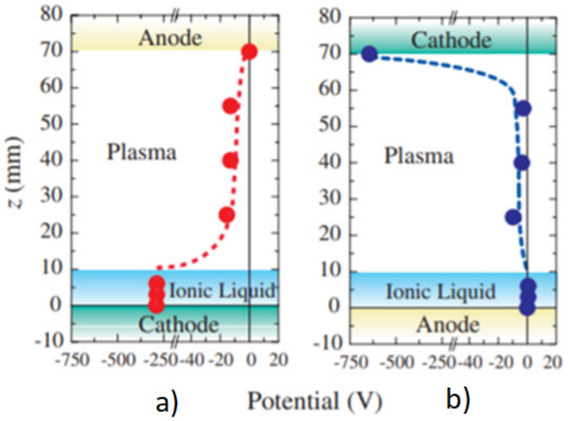

Figure 13. – Plasma potential distribution along the axis of the electrodes from the liquid as a) Cathode and b) Anode [96].

The processes of the plasma-liquid system with an aqueous solution of metal salt as a cathode in an Ar atmosphere is illustrated in Figure 14a. Ar ions are ejected from the bulk plasma toward the liquid surface regarding to the large cathode voltage. Then these energetic ions collide with the liquid's surface, generating secondary electrons and decomposing the liquid's components to form various reducing species such as H, OH, H_2, H_2O_2, and hydride (H^-). Additionally, these secondary electrons can dissolve into the water to form hydrated electrons (e_{aq}^-) with a powerful reducing ability.

Moreover, droplets of the solution form at the plasma-liquid interface and in the bulk plasma due to sputtering or evaporation transport. Due to the high surface-to-volume ratio of the droplets, they can interact with more electrons than the liquid at the surface, resulting in a more effective reduction of metal ions in the droplets.

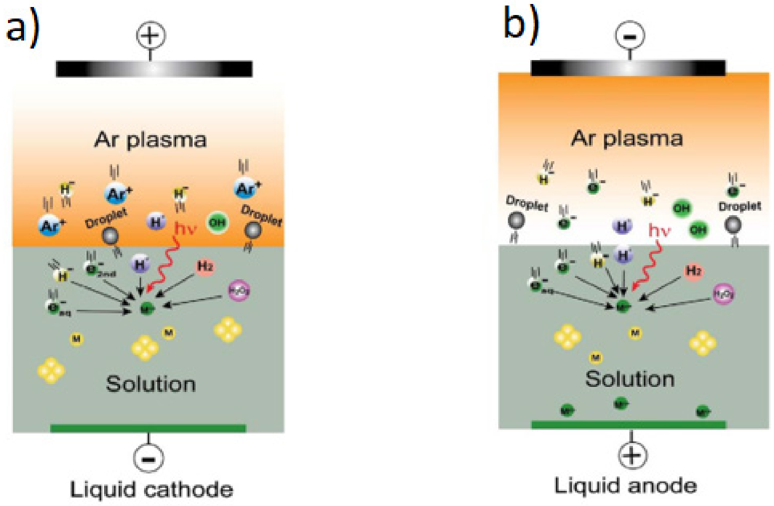

Figure 14. – Nanomaterial synthesis processes for the liquid cathode and liquid anode [96]

Due to the absence of a voltage drop at the liquid surface in the liquid-anode case, electrons from the bulk plasma are deposited on the liquid (e_{aq}^{-}). As with liquid cathode, solution decomposes, and the same species can be generated in bulk plasma but at a lower yield than in liquid cathode. As a result, the reducing efficiency is more significant in the liquid cathode case than in the liquid anode case, which can be influenced by the final nanomaterials' size and structure. Also, in both configurations, oxidizing species such as atomic O, O_3, and OH radicals can be generated at the interface and dispersed into the liquid.

Furthermore, energy constraints and the lifetime of reducing species can affect the synthesis of nanoparticles in plasma over liquid systems, which are caused by their penetrating a specific depth of the bulk liquid and performing chemical reactions. In general, reducing species can be classified into two types: a) short-lived reducing species such as free electrons, e_{aq}^{-}, secondary electrons, and H- that vanish or decay rapidly after the plasma irradiation is stopped, and b) long-lived reducing species such as H_2 and H_2O_2, which can persist in the liquid for an extended period. By utilizing these two types of reducing species, it is possible to control the nucleation and growth processes of the synthesized nanomaterials [97].

1.4.2.2- Plasma indirectly coupled with liquid

Another type of plasma over a liquid system that is frequently used is the plasma jet, which is indirectly coupled to a liquid. Typically, the jet comprises bullet-shaped plasma volumes that travel at 10^5 m/s through the gap distance [98].

As illustrated in Figure 15, the plasma bullet propagates toward the gas-liquid interface when it appears. After the first plasma bullet diminishes, a second bullet forms above the gas-liquid interface and begins propagating in the opposite direction of the first.

Evidently, the second bullet ignites due to the locally generated electric field created by the charge deposited on the gas-liquid interface by the first plasma bullet. This induced electric field is higher than the gas's breakdown threshold at atmospheric pressure. Thus, the charge deposited on the liquid surface can re-ignite the plasma.

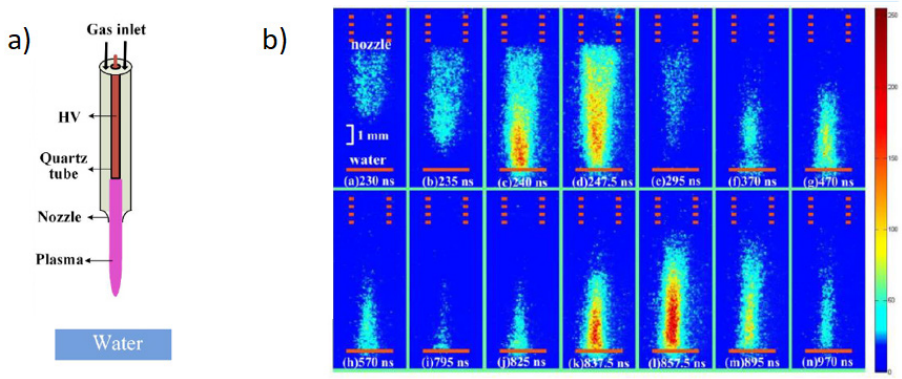

Figure 15. – a) Schematic of the plasma jet over the liquid b) Temporal emission behavior of the plasma bullet in one voltage pulse cycle [98]

This setup can produce a variety of different types of nanoparticles. Kondeti et al. synthesized Ag nanoparticles without using a surfactant using an RF atmospheric pressure plasma jet [99]. Xie et al. synthesized aqueous Au nanoparticles using an AC and a pulse-power-driven plasma jet [100].

It should be noted that while plasma is typically in contact with the liquid in linear jets, plasma and liquid are coupled indirectly in cross-field jets, meaning they are not electrically connected (Figure 16). There are significant differences between linear and cross-field plasma jets in the reactive species produced in the liquid. Kushner et al. modeled these two cases in comparison to demonstrate the influence of these two systems on the reactive species formed in the water [101].

Reactive species can be formed in linear plasma jets via photolysis, direct charge exchange reactions with water, or direct solvation of electrons, and the longer the plasma remains on the liquid surface, the more reactions charged species are formed. However, indirect plasma jets generate a flux of streamers that generate electrons and ions far from the nozzle, and the plasma liquid interaction is primarily due to neutral species that form remotely from the water and are convected and diffused to the liquid surface. The delivery of these neutral species to the water is dependent on fluid dynamics, specifically on turbulence, which increases the dwell time of neutral species at the water's surface and thus increases the possibility of their solvation [102, 103].

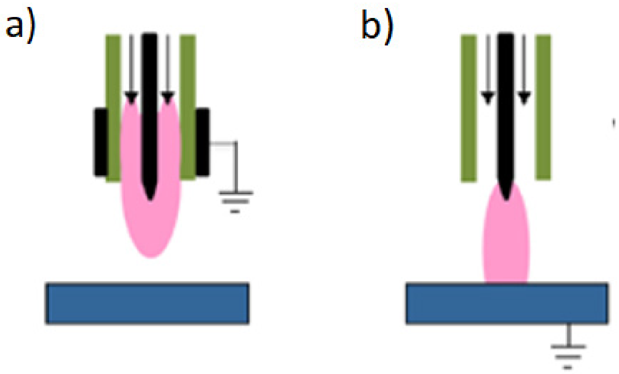

Figure 16. – a) Indirect and b) Direct plasma jet [104]

In addition to the plasma jet, Figure 17 illustrates additional configurations of indirectly coupled plasma with the liquid used to produce nanoparticles. Figure 17a depicts plasma formation between two metal electrodes, with the liquid in contact with the plasma. Liu et al. successfully synthesized Pt and Au nanoparticles using this setup (from the aqueous solution precursors H_2PtCl_6 and $HAuCl_4$, respectively [105,106]). Mok et al. synthesized RuO_2 nanomaterials using a similar setup and precursor chemicals such as $RuCl_3.xH_2O$ and NaOH [107].

Moreover, Uchida et al. designed dual plasma electrolysis in Figure 17b, using two atmospheric glow discharge plasmas as electrodes in contact with the liquid rather than conventional metal electrodes immersed in a liquid. They used this setup to synthesize an Au-Ag core-shell by mixing metal precursors [108].

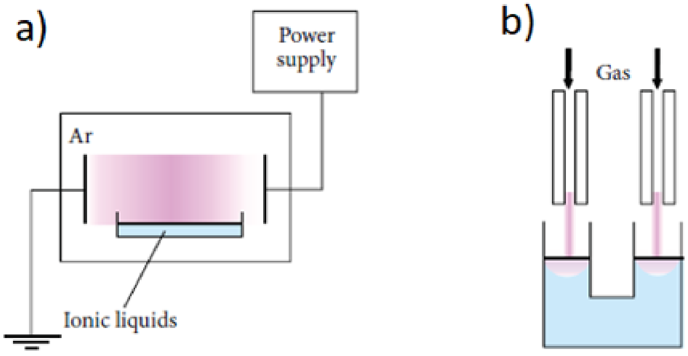

Figure 17. – a) Influence of glow discharge plasma and dielectric [105] and b) Dual plasma electrolysis [108].

1.4.3- Plasma in a multi-phase environment

Since the plasma-liquid interface is the region of interest for chemical and physical processes, the community is keen on increasing plasma-liquid interaction. In this context, two major configurations have been investigated: plasmas in liquid bubbles and plasmas with liquid droplets.

1.4.3.1- Plasma in bubbles in liquid

Discharge formation in externally applied bubbles can be used to increase energy efficiency. The presence of bubbles in a liquid reduces the electrical breakdown threshold, which is determined by the critical value of the reduced electric field E/N, where N is the atom or molecule concentration. The intensity of an electric field's breakdown in a liquid is significantly greater than in a gas. This difference is because the concentration of molecules in a gas at atmospheric pressure is two to three orders of magnitude lower than in liquid [109].

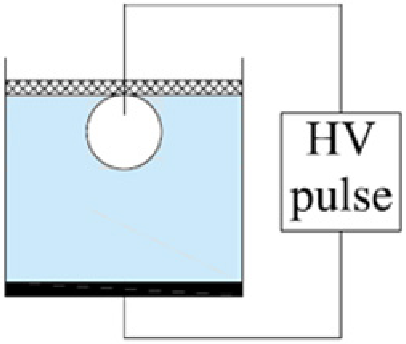

Figure 18. – Electrical breakdown of bubbles in liquid [109]

Figure 18 illustrates a bubble discharge consisting of pulsed electrical discharges in a single bubble immersed in deionized water. Multiple discharges occur within the bubble during the voltage pulse, depositing charge on the bubble's surface. This accumulation of charges on the surface results in the generation of a reverse-polarity discharge during the voltage shut-off period. Thus, in this case, active species are produced by plasma within the bubbles and transported into the liquid via the bubbles.

As a conductivity of the liquid increases, the breakdown voltage of vapor bubbles decreases due to the liquid's decreasing resistance. Additionally, bubble length affects the breakdown of the electrical field, as they decrease with decreasing bubble size. Bruggeman et al. investigated the DC electrical breakdown in air and water vapor bubbles in a capillary tube. They calculated the distribution of electrical fields at breakdown and demonstrated that the electrical field along the bubble's axis of symmetry is smaller than the field near the bubble surface. Furthermore, the bubble surface/tube interface has the strongest electrical field (Figure 19c) [110].

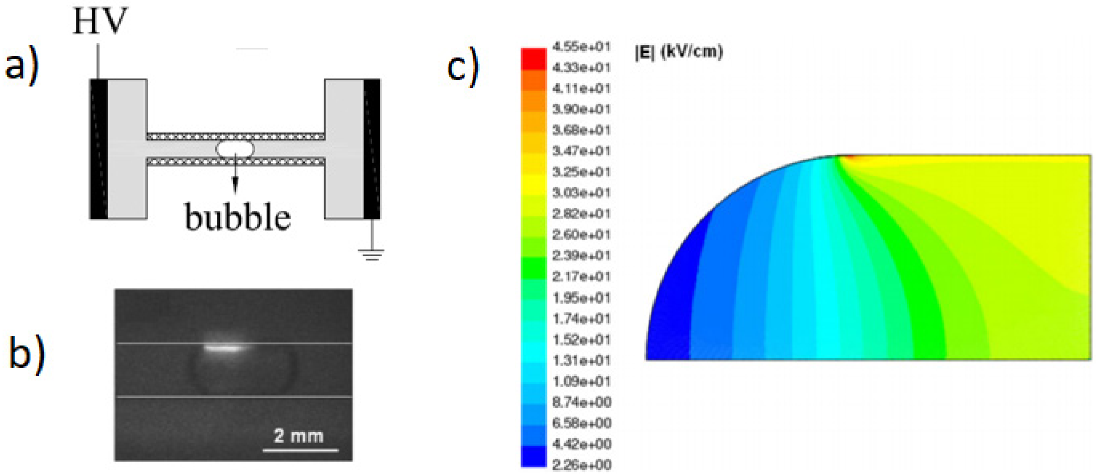

Figure 19. – a) Schematic of the e experimental setup b) Plasma light pattern confined to the bubble surface c) Distribution of the amplitude of the electrical field in a bubble in one-fourth of a section of the bubble [110]

The characteristics of the discharge can be altered by modifying the gas composition and the interelectrode distance. The electron density and energy of electrons reduce as the interelectrode distance increases [111]. Moreover, the electron density is greater (lesser) in gases with a lower (greater) ionization energy.

The position of the bubbles is a critical factor in electrical breakdown. For instance, if gas bubbles form a chain-like structure, the discharge may leap from bubble to bubble and propagate along the bubble chain. The discharge in the connected triple bubbles is more powerful and diffuse than the discharges in the other multi-bubble configurations (Figure 20) [112]. All the factors discussed above for the plasma generation in bubbles within liquids significantly affect the ability of reactive producing species to form various nanoparticles.

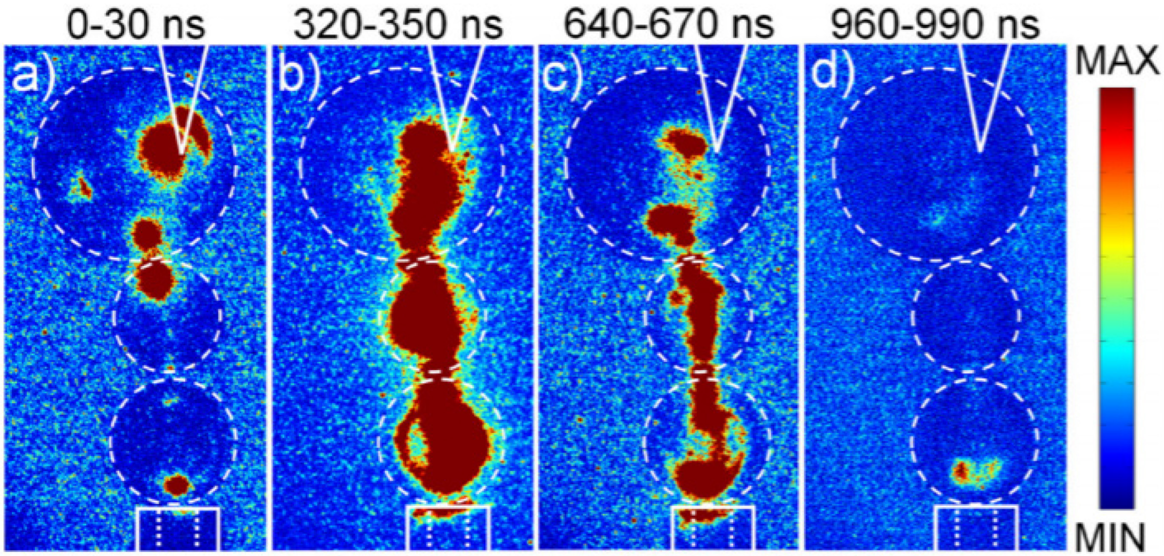

Figure 20. – Time evolution of simultaneous ignitions at multiple points in triple argon bubbles [112].

1.4.3.2- Plasma with liquid droplets

A spray liquid system is a type of plasma generated via multiphase methods (Figure 21). Shan et al. simulated the desolvation of aerosol droplets in a radio frequency plasma and demonstrated that the injection of droplets decreases the temperature of the droplet-occupied space [113]. This temperature decrease results in a delay in the droplet's desolvation process within the plasma, which is an important factor because during this dissolution time, the droplets interact with the plasma, producing reactive species.

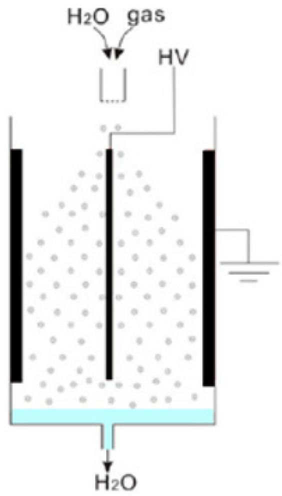

Figure 21. – Wire-to-cylinder spray discharge [113].

Dubinov et al. investigated the forms of the spark discharge plasma channel on droplets. They demonstrated that spark discharges above droplets behaved differently depending on the liquid conductivity. As shown in Figure 22, for a liquid with high electrical conductivity, such as a salt solution, the discharge channel begins at the needle electrode and ends at the top of the droplet; the discharge current then flows into the droplet volume (Figure 22a). However, when a solution with low electrical conductivity is used, such as distilled water, the discharge flows over the droplet surface (Figure 22b), and the surface discharge channel branches as well [114].

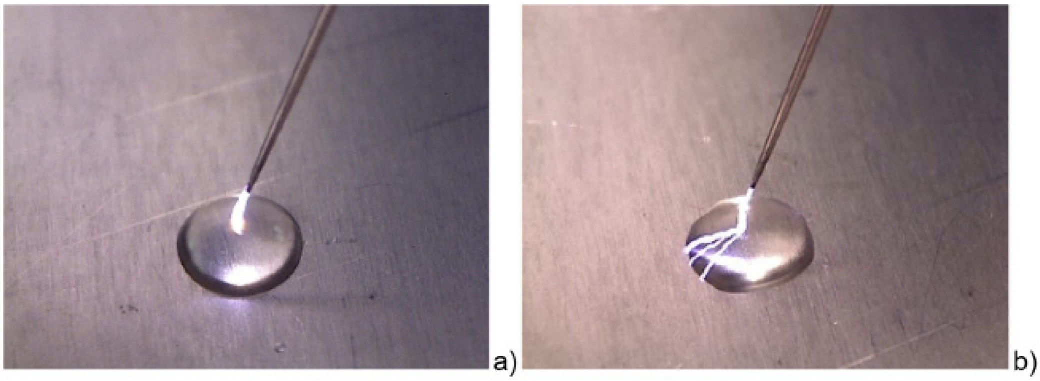

Figure 22. – Forming of discharge channel, a) Above the droplet of high electrical conductivity liquid and b) Over a droplet of a low conducting liquid [114].

Also, they investigated the coalescence and mixing of droplets of various liquids using the spark discharges. As depicted in Figure 23, two droplets of liquid of varying colors (one droplet was coloured with $KMnO_4$) were placed on a dielectric substrate with different distances between their edges, and pin steel electrodes were inserted into both droplets and connected to the high voltage.

The spatial form of the plasma discharge channels depended on the distance between the droplets and the electrical conductivity of the liquid, such that when the electrical conductivity of the liquid was high (Figure 23a), the discharge channel was short and connected the two nearest droplet points along the substrate surface [115]. Furthermore, due to the low electrical conductivity of the droplets (Figure 23b), the plasma channel connected two points of pin electrode entry in the droplets, spread along the droplet’s surface and substrate, and branched as well.

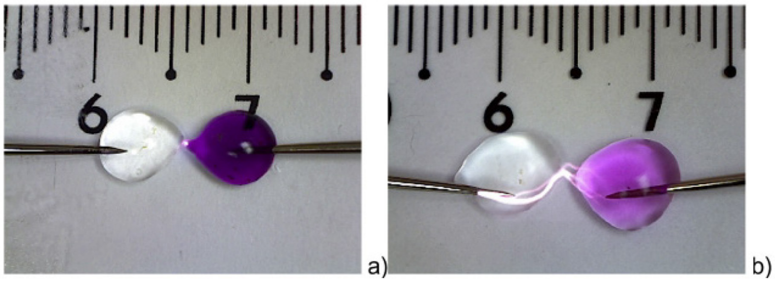

a) b)

Figure 23. – Typical forms of the discharge channels between the droplets a) Short channel and b) Long channel [115].

Figure 24 shows the dynamics of water droplets merging and mixing when a negative voltage pulse is applied. Initially, the droplets are attracted to one another, and spark discharges periodically appear between the droplets' nearest points. The droplets are then drawn out until a channel of approximately 0.5 mm in width is created. These are referred to as water bridges [115,116]. Figure 24c depicts the passage of a small fraction of the MnO_4^- ions across the bridge to the other electrode via a narrow flux. The bridge width and the width of the MnO_4 ion flux then increased abruptly in Figure 24d. Finally, a uniform distribution of ions in both droplets is established (Figure 24e, f).

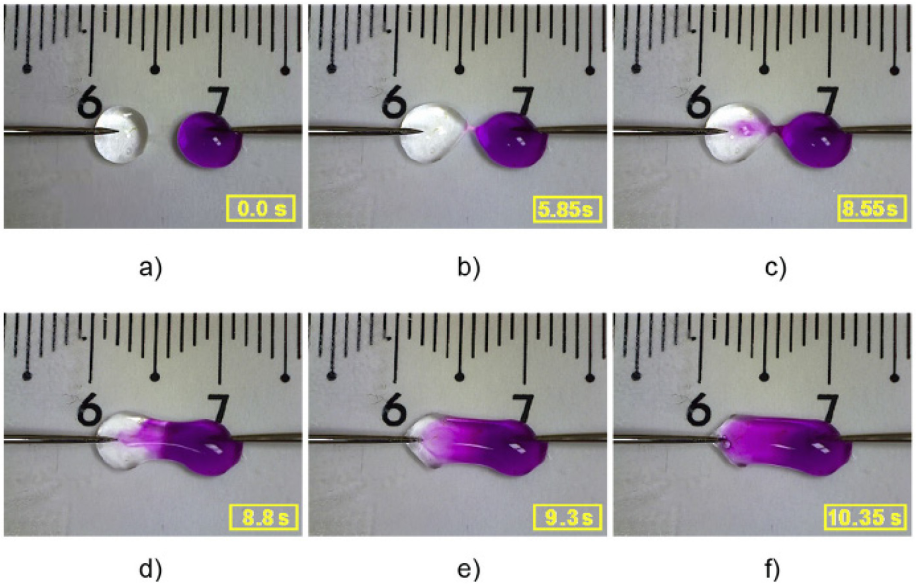

a) b) c)

d) e) f)

Figure 24. – Images of the water droplets merging process and mixing their contents [115].

On the other hand, the process of combining droplets of two different liquids is quite different. As displayed in Figure 25, the first step in the process of merging a glycerin droplet with a droplet of colored water is for the droplets to be drawn toward one another, forming a liquid bridge. In this instance, no mixing occurred (Figure 25c), and gas bubbles were formed (Figure 25d). These bubbles are lined up in a glycerin foam column (Figure 25e), which is then filled with colored water (Figure 25f), at which point the evolution of droplets comes to a halt.

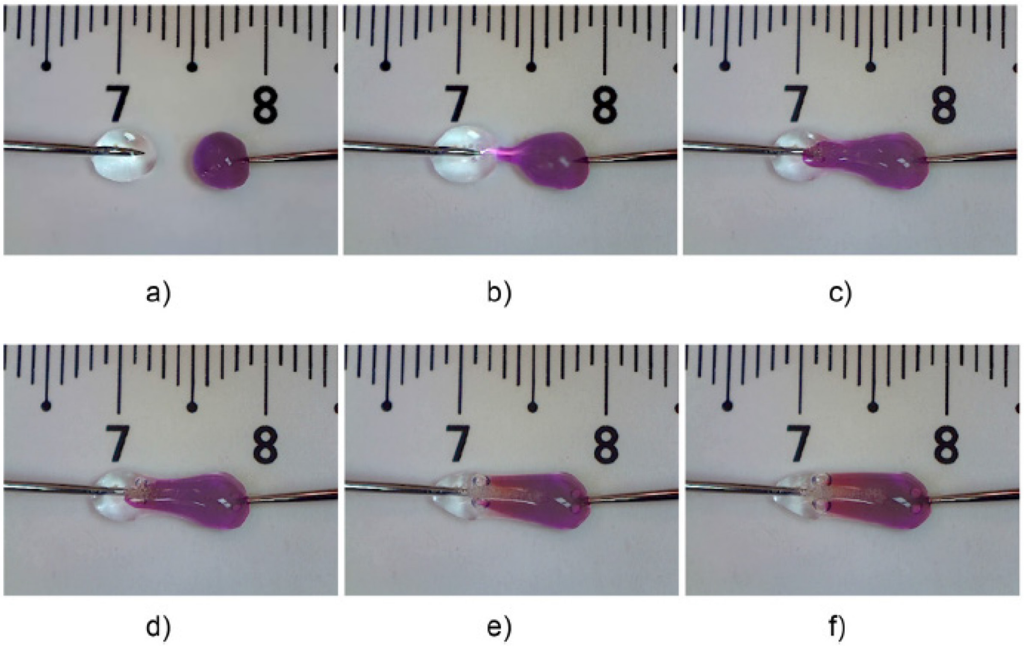

a) b) c)

d) e) f)

Figure 25. – Images of the process of merging glycerin and tinted water droplets without mixing their contents [115,116].

In summary, this chapter reviewed most common plasma systems, in particular plasma-liquid systems, that have potential in the production of nanoparticles. The next chapter will introduce the discharges in a mixture of two immiscible liquids which is a novel plasma-liquid configuration.

Chapter 2 – Discharges in a mixture of two immiscible liquids

This section describes in detail the discharge process in multiple liquid systems. The primary objective of implementing such systems is to increase treatment efficiency while reducing energy consumption. These electric discharges in multi-liquids can be used for various purposes, including water purification, fuel reforming, and nanomaterial synthesis. Since this is the application developed in this thesis, only this latter is discussed in detail below [117,118].

As mentioned previously, the synthesis of nanomaterials via electrical discharges in a single liquid has been extensively studied over the last decade. Such discharges have been used to synthesize metals such as Ag, Au [119]; metal oxides like ZrO_2 nanoparticles by a pulsed plasma in three different dielectric solutions: distilled water, hydrogen peroxide (30.0%), and ammonia solution (28.0%), or CuO nanostructures using electrical discharges between copper electrodes immersed in deionized water [120, 121]; organosilicon (e.g., silicon oxycarbide nanoparticles produced by electric discharge in liquid HMDSO, TEOS, and TMCTS) [122]. Discharges in a liquid have also been demonstrated to be an efficient method for synthesizing various structures, including core-shell nanoparticles like for example copper-carbon particles formed by spark discharges between two copper electrodes immersed in heptane, cyclohexane, or toluene[123], or producing nanocomposite materials such as carbon-coated TiO_2 nanoparticles using graphite electrodes immersed in water containing TiO_2 or forming Pt nanoparticles embedded in a carbon matrix by electrical discharges between Pt electrodes immersed in n-heptane [124,125], as well as synthesising nanoalloys like cobalt-nickel by ignition of discharge between pure cobalt and nickel electrodes immersed in liquid nitrogen [126].

In the following, the properties of electrical discharges in multiple liquids systems will be introduced.

2.1- Discharge at the interface of two immiscible liquids

Hamdan et al. (2016) demonstrated that the best way to investigate the role of a liquid-liquid interface at the macroscopic level is to use two immiscible liquids [127]. The initial research on this subject used distilled water and heptane (Figure 26). The authors demonstrated that the position of the anode pin relative to the interface significantly affects the discharge dynamics.

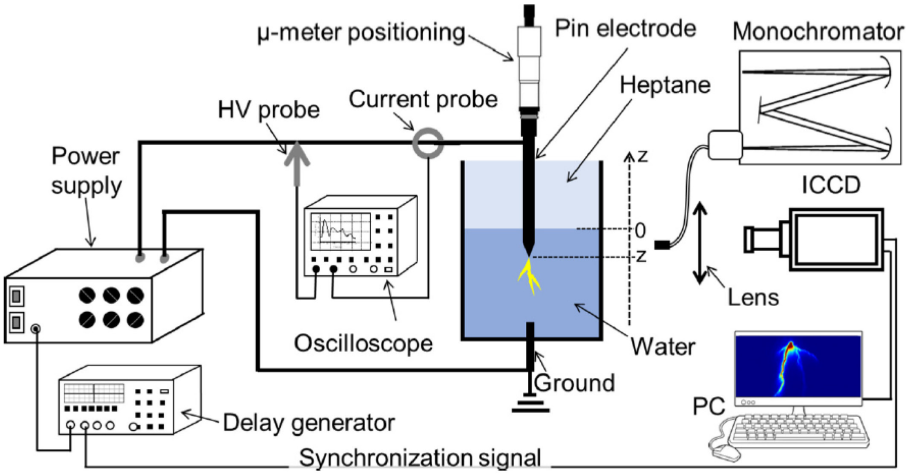

Figure 26. – Schematic of the experimental setup used to produce pulsed nanosecond discharges in solution [128]

By adding a layer of n-heptane over the distilled water and approaching the pin electrode to the interface, the percentage of successful electrical discharges (discharge probability) was significantly increased. However, electrical discharges did not occur in water alone under the same conditions (Figure 27).

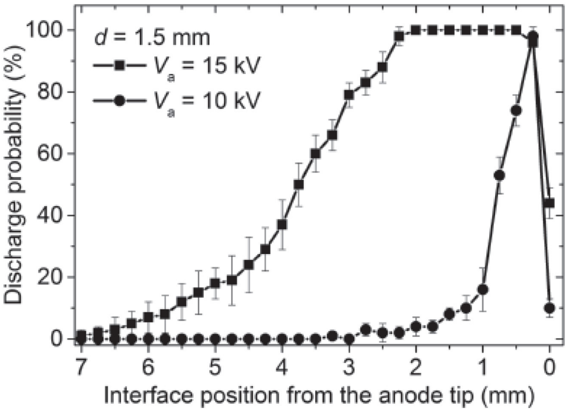

Figure 27. – Discharge probability as a function of the position of the interface from the electrode tip [127]

An ICCD camera was used to capture the spatial distribution of the light emitted by the discharge to investigate the plasma's morphology. According to the setup, z=0 represents the interface position, and +h represents the distance between the interface and the electrode's tip while immersed in water. As shown in Figures 28a-c, decreasing h from 6.7 to approximately 3 increases the region of plasma emission. Further lowering of h causes filaments (streamers) to form in the water (Figure 28d-f). Plasma filaments propagate horizontally, along to the interface when they are very close to it. The increased of discharges occurrence and number of plasma filaments/volume is explained by the enhancement of the electric field caused by the difference in the dielectric permittivity of the two liquids (2 for n-heptane and 80 for water).

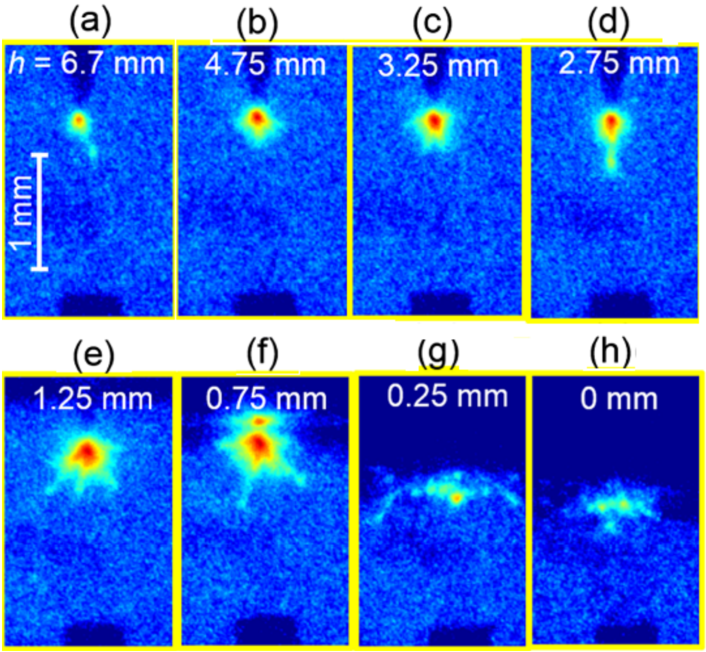

Figure 28. – ICCD images of electric discharges according to the interface position [127]

The simulation shown in Figure 29 indicates that as the pin electrode approaches the liquid interface, the intensity of the electric field increases, reaching a maximum when the pin reaches the interface. The discontinuity of dielectric permittivity causes this intensification of the electric field [127,129]. The tangential components of an electric field at an interface, $E_{x,y}$, should be identical ($E_{x,y,water}=E_{x,y,n\text{-}heptane}$). However, the electric flux density in the normal component direction, E_z, should be conserved, such that $\varepsilon_{water}E_{z\ water} = \varepsilon_{heptane}E_{z,heptane}$. As a result, the normal component of E is amplified by the ratio of the permittivity of the two liquids, which equals $\varepsilon_{water}/\varepsilon_{n\text{-}heptane} = 80/2$.

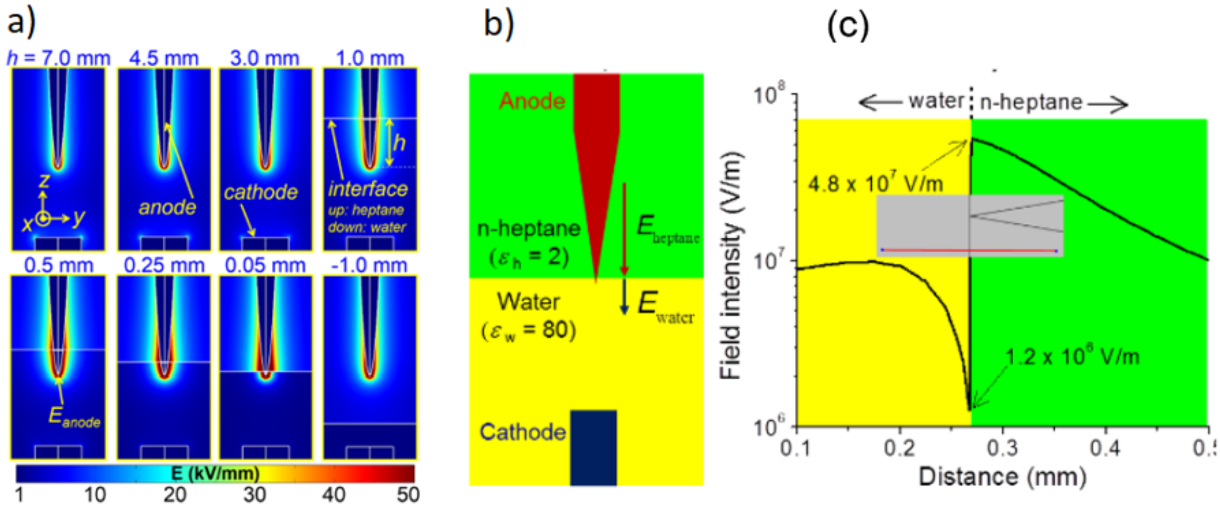

Figure 29. – a) COMSOL simulations of electric field intensity. the horizontal yellow line indicates the position of the interface [127] b) The experimental schematic and c) The diagram of the measured electric field at the interface [130]

2.1.1- Effects of water conductivity on discharges in multiple liquids

Recently, the effect of water conductivity in the range of 10 to 5000 µS/cm on discharge behavior was addressed [128]. The previous section discussed the case of low conductivity in water (10 µS/cm), and this section presents the electrical characteristics of a typical discharge in water (Figure 30 a, b). As depicted in Figure 30a, the voltage waveform remains constant for different electrode positions, i.e. there is no drop for the pin in water (z=-4mm), the pin at the interface (z=0 mm), and the pin on the heptane side (z=2.5 mm). However, at the interface (z=0), a series of current peaks with values can be seen. Notably, the initial peak at t~0 corresponds to the displacement current induced by increasing the voltage (Figure 30b), and as shown in the figure 30b, the peak's value changes by the gap distance because of the gap capacitance variation.

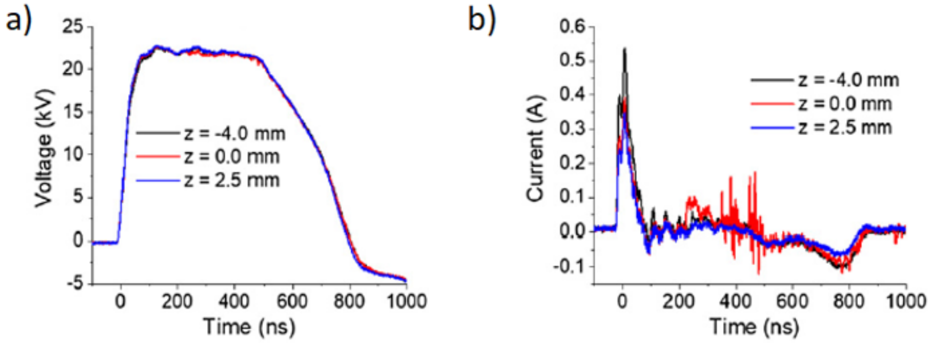

Figure 30. – a) Voltage and b) Current waveforms of discharges in distilled water for positive polarity as a function of z [128]

Figure 31a shows the effect of increasing water electrical conductivity as a function of electrode gap. Increasing the conductivity to 100 µS/cm, it possible to conduct more discharges in water and away from the interface. Further increase to 500 µS/cm reduces discharge occurrence in water far from the interface, but it remains relatively high (100%) close to the interface. Electrical characteristics (Figures 31b and c) also strongly correlate with water's electrical conductivity. Voltage plateaus and voltage drop for both 50 and 100 µS/cm are almost the same, while for 500 µS/cm both are decreased. Current waveform, as shown in figure 3c, shows rising of the discharge currents as the conductivity increases. It should be noted that numerous spikes are observed at lower electrical conductivities but not at 500 µS/cm, indicating that the discharge mode has changed.

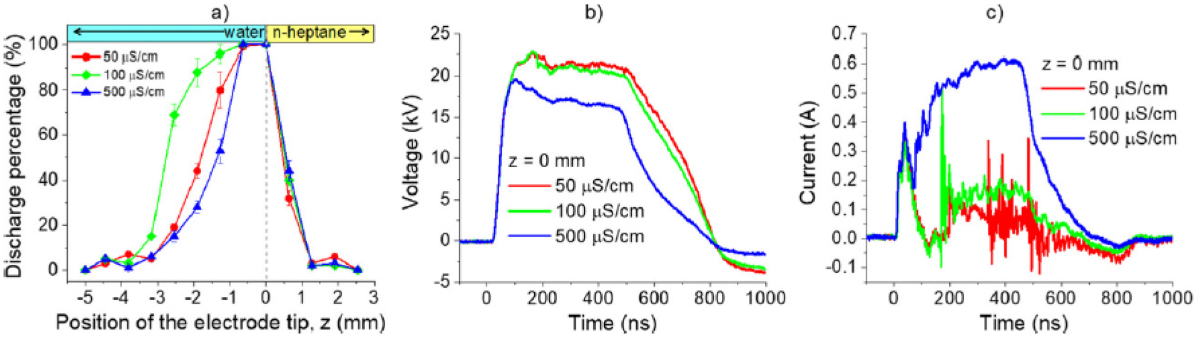

Figure 31. – a) The percentage variation of successful discharges in water as a function of electrode position relative to the liquids' interface (z=0) at various electrical conductivities. b,c) Waveforms of the voltage and current discharges at the heptane/water interface under various conductivity conditions [128]

By increasing conductivity to 5000 µS/cm, the discharge probability was increased by closing the electrode tip to the heptane side, and the voltage-current waveforms are similar to those at 500 µS/cm (Figure 32).

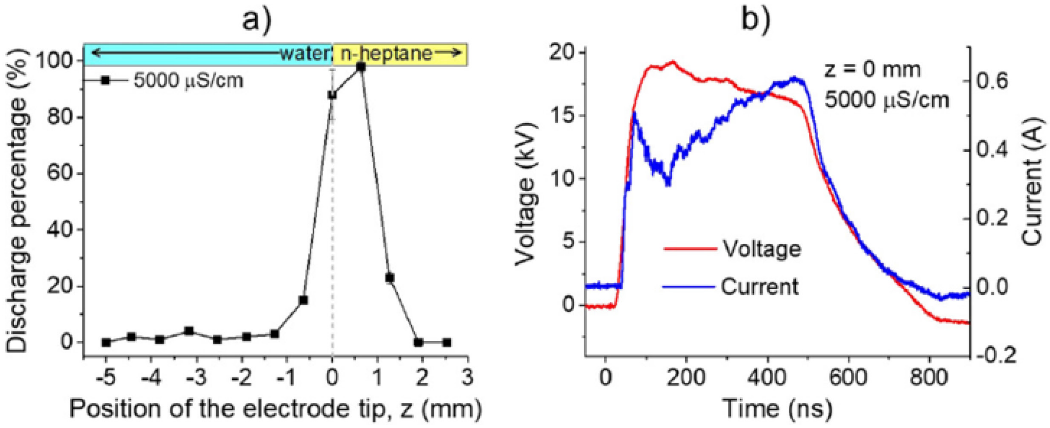

Figure 32. – a) The percentage variation of successful discharges (positive polarity) produced in water as a function z, at 5000 µS/cm. b) Voltage and current waveforms of a plasma generated at the heptane/water interface (z = 0), at 5000 µS/cm [128]

2.1.2- Discharge morphology of multiple liquid system with different water conductivity

By examining the ICCD images of the plasma emissions (Figure 33) produced under varying z and electrical conductivity conditions, it is possible to deduce that the discharges produced by positive polarity at 50 and 100 µS/cm have a filamentary shape and, as the anode pin approached the interface, the plasma filaments became longer and more intense.

In addition to vertically propagating filaments toward the cathode, horizontally propagating filaments can be formed. Furthermore, unlike deionized water (10 µS/cm), these vertical filaments are longer than horizontal filaments. Moreover, far from the interface, more discharges occur on the water side than on the heptane side, and the vertical filaments formed in heptane were significantly shorter in length than the horizontally propagating filaments.

The filamentation phenomenon is suppressed at 500 µS/cm water conductivity, and the filaments were more intense, shorter, and broader than in lower conductivity cases. At z = 0.6

mm, as illustrated in Figure 33c, the filaments were short, and the emission zone had an elliptical shape rather than a filamentary shape.

At a conductivity of 5000 µS/cm, the plasma filamentary shape is wholly suppressed, and only one plasma emission zone can be observed on the heptane side (Figure 33d). The emission intensity was relatively low on the water side (z=-0.6 mm), but by approaching to the interface the plasma emission intensified and took on an elliptical shape, becoming more intense on the heptane side.

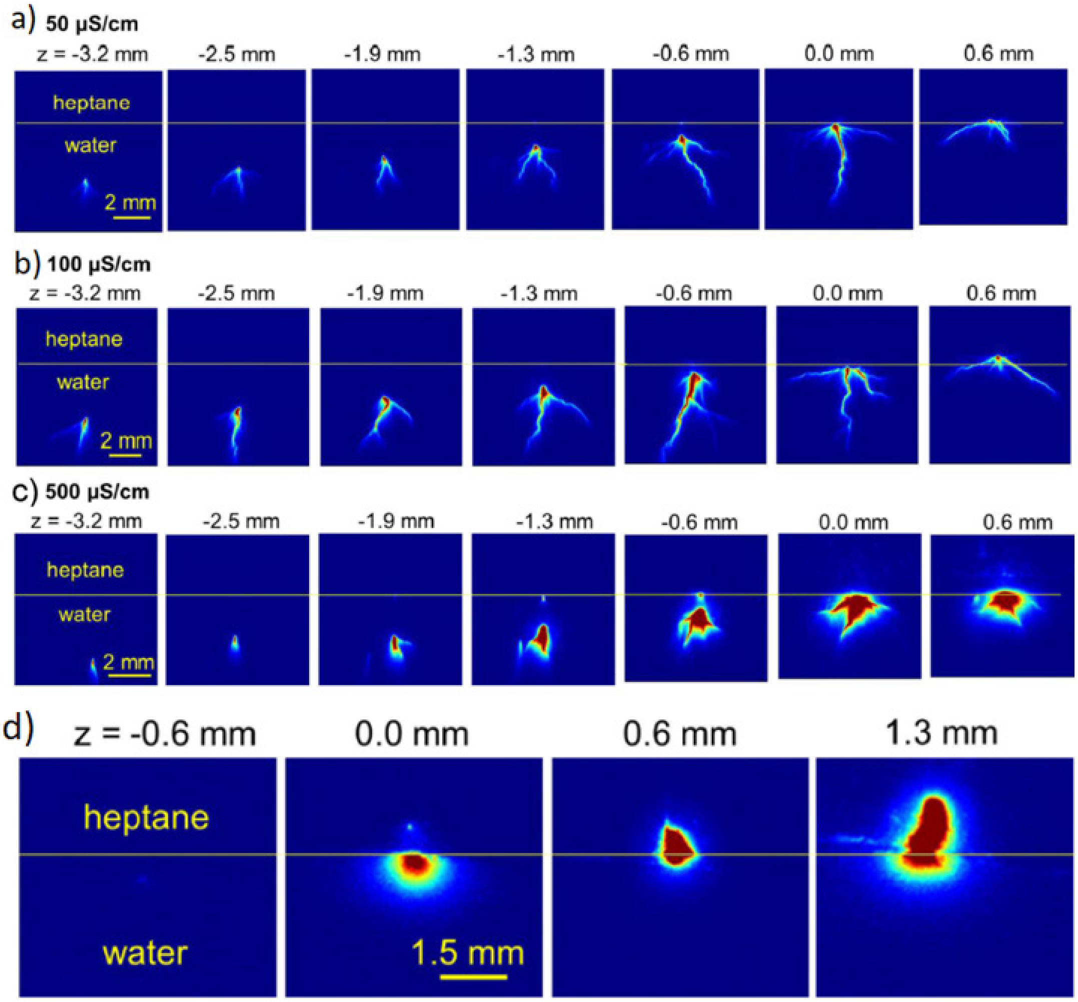

Figure 33. – ICCD images of the discharge emissions (positive polarity) produced in water at a) 50, b) 100, and c) 500 µS/cm d)5000 µS/cm [128]

Combination of two reasons can be considered to explain this non-uniform behavior of plasma due to an increasing electrical conductivity: 1) the presence of free ions in water resulted in a decrease in the number of discharges by increasing the conductivity of the water; and 2) as previously stated, as the electrode pin gets close to the interface, the electric field at the pin is highly intensified and compensates the decrease of discharge occurrence caused by increased conductivity.

Another explanation which can describe these differences in plasma dynamics for low and high conductivity is related to the discharge dependency on flow of electrons. At positive polarity, the electrons are flow from the liquid to the pin electrode(anode) and leaving a positive space charge behind. Therefore, due to the low concentration of free ions in the liquid at low conductivity, space charge affected the propagation of streamers. On the other hand, at high conductivity, because of the large number of ions, the effect of space charge on filament propagation is reduced, and a localized plasma rather than a filamentary-like plasma can be observed.

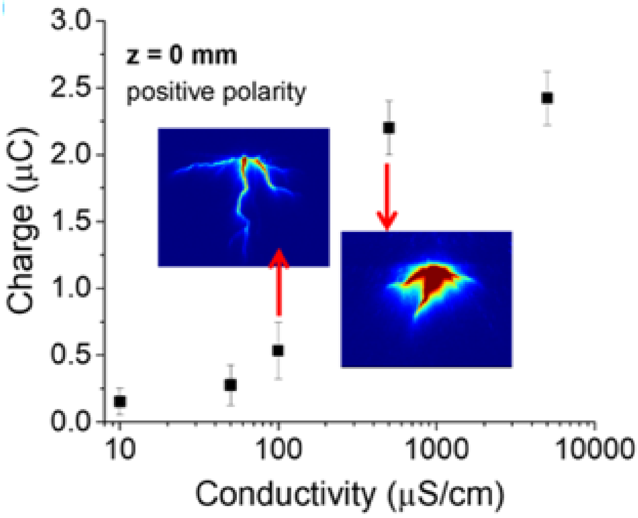

Figure 34. – Variation of the injected charge of discharges for positive polarity and the water/heptane interface as a function of water conductivity [128]

The injected charges and electron density are enlarged by increasing the conductivity of the water. According to Figure 34, for low conductivity (<100 μS/cm) and high conductivity (>500 μS/cm), the injected charge is approximately 0.2 μC and 2.2 μC, respectively. According to the charge value and different plasma shapes in low and high conductivity at positive polarity, it can be concluded that discharges tend to propagate in streamer and spark modes at low and high-water conductivity, respectively. Moreover, optical emission spectra acquired under various conductivity conditions demonstrated that C_2 (Swan band from ~480 to 590 nm) is easily identifiable at low conductivity (streamer mode); however, at high conductivity (spark mode), the lines become so broad that only one broad band is visible (Figure 35a).

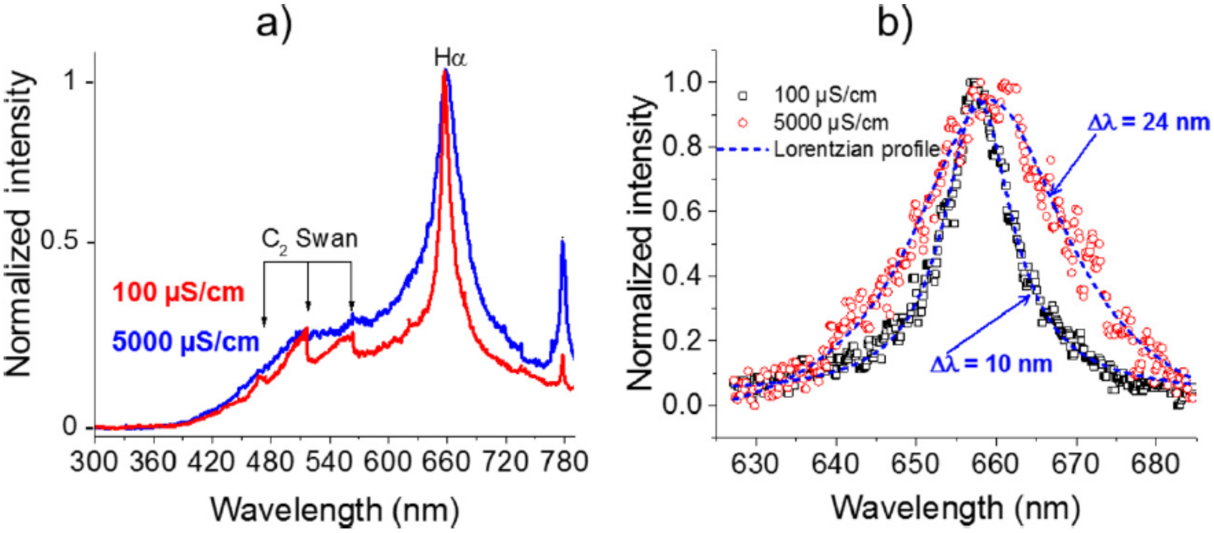

Figure 35. – a) Optical emission spectra of discharges (positive polarity) at the water/heptane interface for two conductivities: 100 and 5000 µS/cm, b) H_α line profiles and the corresponding Lorentzian fits at 100 and 5000 µS/cm [128].

The broadening of the Hα line results from the Stark effect, which is ascertained by collecting the optical emission spectrum (Figure 35b). Lorentzian functions were used to fit the acquired profiles [131-133]. Using $n_e(cm^{-3}) = 8.83 \times 10^{16} \times \Delta\lambda(nm)^{1.6005}$, where $\Delta\lambda$ is the full width at half maximum of Hα, the value of $n_e$is determined that can have different value of 3.5×10^{18} and 1.4×10^{19} cm^{-3}, depending on the water conductivity [134].

2.2- Producing nanoparticles using plasma in multiple liquid systems

The ability to synthesize nanoparticles from a mixture of multiple liquids has been demonstrated by either chemical or plasma-based ways. For example, semiconducting polymer (methyl-substituted ladder-type poly (para-phenylene)) nanospheres have been produced via the nanoemulsion process as describe in the following. Nanoemulsions are stable emulsions consisting of stable droplets with a size of 50-500nm formed by shearing a system containing oil, water, a surfactant, and an insoluble compound. Thus, chloroform solutions of semiconducting polymer (para-phenylene) were emulsified in water using sodium dodecyl sulfate (SDS) as a surfactant to produce para-phenylene nanoparticles.

Additionally, using the same method, nanoparticles of various semiconducting polymers such as main-chain polyether, F8BT, and PFO can be produced by dissolving them in $ChCl_3$ and adding an aqueous SDS solution (Figure 36) [135].

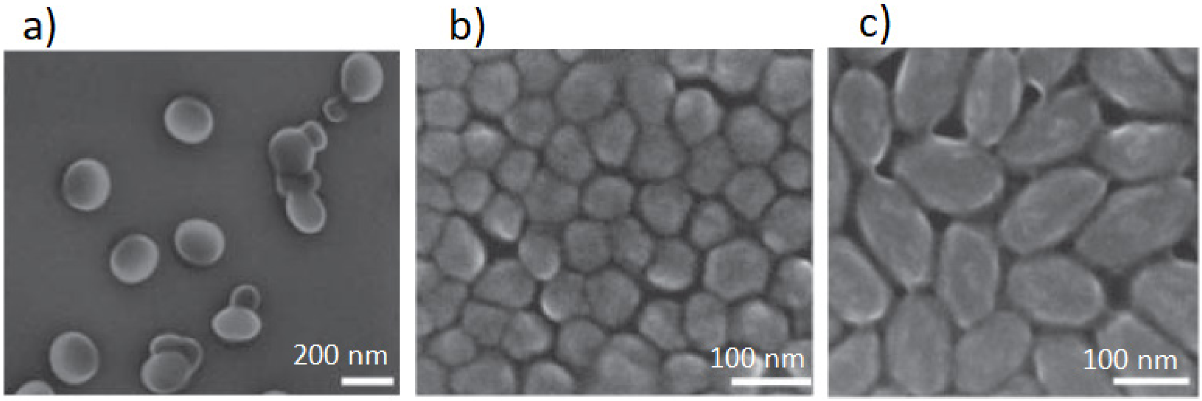

Figure 36. – SEM images of different size and shape of polymer nanoparticles a) main-chain polyether nanoparticles b) F8BT nanoparticles c) PFO nanoparticles [135].

Coupling an electrical discharge with an emulsified liquid is a new field with limited knowledge. For example, Kelgenbaeva et al. demonstrated that electrical discharges between two Fe electrodes in a water-toluene emulsion produced pure α-Fe nanoparticles via electrode erosion (Figure 37a). Also, they demonstrated that the ratio of toluene to water in an emulsion affects the purity and size of Fe nanoparticles [136]. Although the authors utilized an emulsified medium, the role of the liquid-liquid interface on the synthesis remains unknown, and the synthesis is mainly due to electrode erosion.

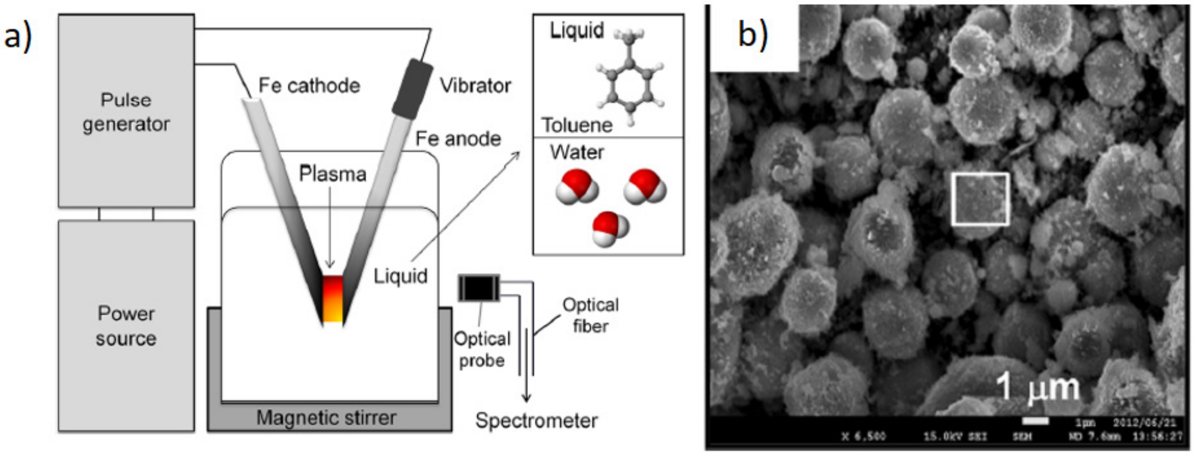

Figure 37. – a) Experimental setup of pulsed plasma between Fe electrodes immersed in water–toluene b) FESEM images of Fe nanoparticles [136].

It was possible to sustain discharges at the interface in a system where a static interface was created by mixing liquid hexamethyldisilazane (HMDSN) and water (Figure 38a). As shown in Figure 38b, after approximately 5 minutes of discharge, the color of the liquid interface changed to a dark tan, indicating that the liquid was transformed, and nanoparticles were formed. Following evaporation of the colored liquid, an off-white powder (84 mg) was extracted, indicating a high production yield [129]. Another advantage of this system is that erosion of the electrode, which is the basis for synthesizing nanomaterials in plasma in a single liquid system, is avoided during plasma treatment, allowing to produce highly pure nanomaterials.

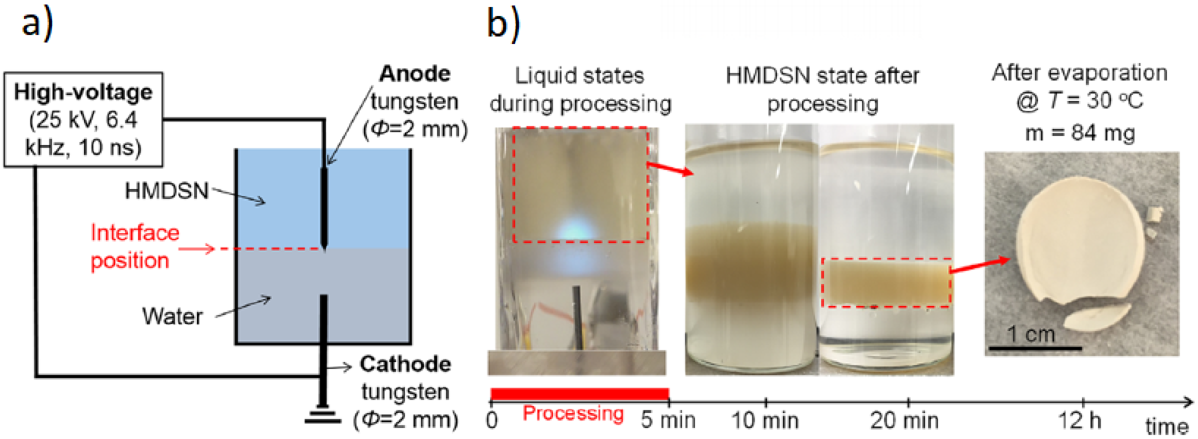

Figure 38. – a) Schematic of the experimental setup b) The liquid states during and after processing and synthesized materials [129]

The SEM analysis of the produced nanomaterials lied on the Al substrate revealed the formation of two types of materials: gel-like materials with nanoparticles embedded in a homogeneous matrix, and nanoparticles with an average size of 30 nm dispersed on the film's surface (Figure 38d).

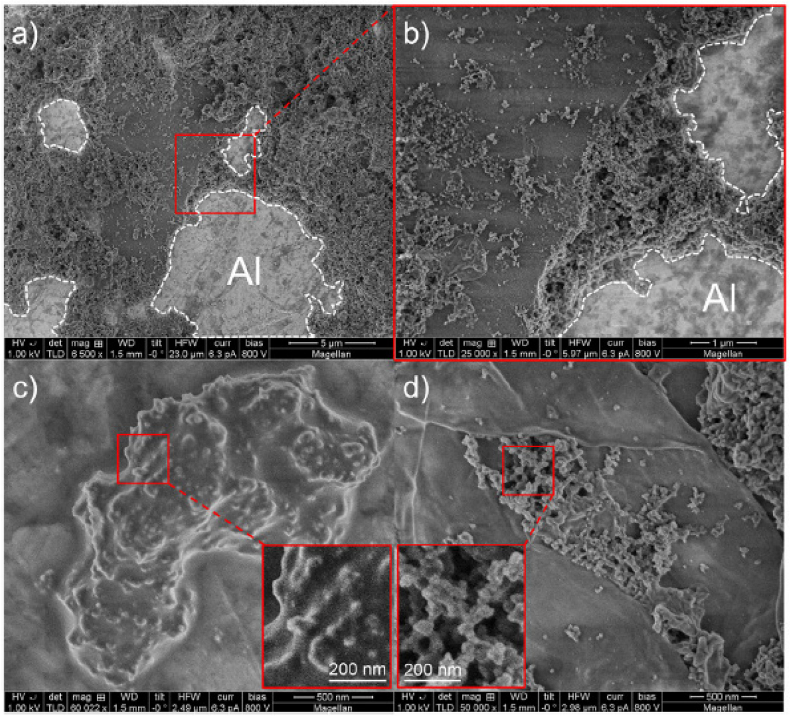

Figure 39. – a,b,c) SEM images of nanoparticles deposited onto an aluminum substrate and d) a gel-like material and nanoparticles dispersed on the surface of a sheet [129]

Sustaining discharges at the n-heptane/water interface resulted in the decomposition of n-heptane (and water) and the formation of carbon-based materials in a very similar setup [130]. Figure 40 illustrates the morphology of the synthesized material.

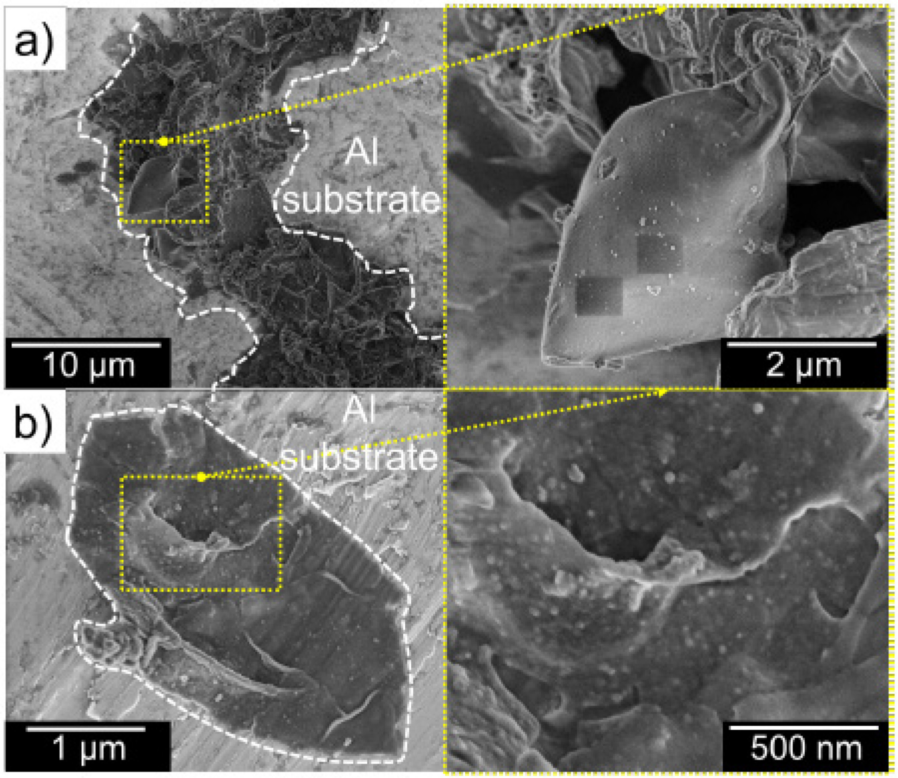

Figure 40. – SEM images of the as-synthesized material deposited onto an aluminum substrate a) Multiple sheets b) A single sheet decorated by nanoparticles [130]

In summary, this chapter described a novel plasma-liquid configuration, that is plasma in two immiscible liquids. The position of the electrode pin regarding the interface plays a major role on the plasma dynamics, as the interface strongly influences the electric field distribution. The conductivity of a solution has also a major role on the discharge mode, as it allows transition from streamer (at low conductivity) to spark (at high conductivity). In the next chapter, we will focus on the spark discharges but, instead of using KCl, we will use silver nitrate to evaluate the feasibility of Ag nanoparticles production in such a novel configuration.

Chapter 3 – Spark discharges in liquid heptane in contact with silver nitrate solution: investigation of the synthesized particles

3.1- Introduction

In this chapter, we characterize the produced nanoparticles using a novel plasma-liquid system in which a spark discharge is used to generate plasma in a liquid that is in contact with another liquid. In this system, a spark was produced between a pin electrode immersed in a dielectric liquid (heptane) and the surface of a conductive solution (water + silver nitrate). This configuration guarantees an interaction between the high-density plasma (spark in heptane) and the solution that contains silver ions, and so, we used it herein to synthesize nanomaterials under two conditions of pulse width.

We note that this chapter is part of a paper that has been recently published in Plasma Processes and Polymers: Mohammadi, K., & Hamdan, A. (2021). Spark discharges in liquid heptane in contact with silver nitrate solution: Investigation of the synthesized particles. *Plasma Processes and Polymers*, e2100083. https://doi.org/10.1002/ppap.202100083

The following sections, including Experimental setup, Results and Discussion, are taken from the published article.

The author of this thesis (K. Mohammadi) has conducted the experiments, characterized the materials, and wrote the first draft of the article.

3.2- Experimental setup

As shown in Figure 41, the experimental setup consists of a ~10-cm-long quartz tube with inner and outer diameters of 17 and 19 mm, respectively. The tube was filled with 6 mL of aqueous solution and 3 mL of n-heptane, and since the two liquids are immiscible, a stable interface was obtained. The upper electrode, a carbon rod (99.99% pure; Goodfellow) that is mechanically polished to a curvature radius of ~10 µm, was immersed in heptane, and the distance between its tip and the interface was kept at ~1 mm. Meanwhile, the lower electrode, a carbon rod that is polished to a flat surface, was placed in the conductive solution at 3 mm below the interface. A positive high voltage was connected to the upper electrode, while the lower electrode was connected to the cathode. Although the position of the cathode in the solution does not influence the results, it must be placed far enough from the interface so that the discharge does not reach it. Using this configuration, spark discharges were sustained in heptane between the anode tip and the surface of the solution. To prepare the conductive aqueous solution (electrical conductivity of ~5 mS/cm), silver nitrate (from Sigma Aldrich) was dissolved in distilled water at the concentration of 40 mM.

The discharge was ignited using a nanosecond positive pulsed generator (NSP 120-20-P-500-TG-H, Eagle Harbor Technologies). The amplitude of the applied voltage was 22 KV, and two pulse widths were tested: 100 and 500 ns. The discharge repetition rate was set to 10 Hz, and the duration of the experiment was 30 min. The electrical characteristics, voltage and current, of the discharge were measured using a high-voltage probe (P6015A, Tektronix) and a current coil (6585, Pearson), respectively. Both probes were connected to an oscilloscope (DPO5420B, Tektronix) in order to record the voltage and current waveforms.

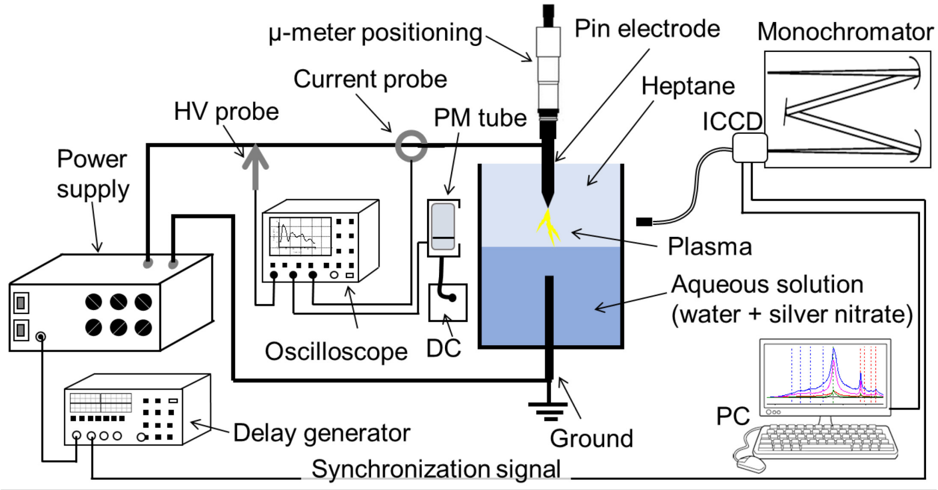

Figure 41. – Scheme of the experimental setup used to generate discharges in liquid heptane that is in contact with silver nitrate solution.

The radiation (~300–800 nm) emitted by the discharge was detected using a photomultiplier (PM) tube (R636, Hamamatsu), and a monochromator (Acton 2750) was used to acquire the emission spectra. The intensity of each optical transition was recorded by an ICCD camera (PI-MAX from Princeton Instruments). Light emission measurements were carried out using the 300 lines/mm grating blazed in the visible range. A delay generator (Quantum Composers Plus 9518 Pulse Generator) was used to ensure synchronization between the ICCD camera and the voltage pulse.

The synthesized nanostructures were characterized using a Transmission Electron Microscope (TEM, JEOL JEM-2100F) operated at 200 kV. For this purpose, the liquid samples collected after discharge were sonicated for 5 min then drop casted in TEM grids endowed with a lacey C-film (Electron Microscopy Science). The nanostructures in both liquids were subsequently analyzed by bright field TEM imaging and Electron Dispersive Spectroscopy (EDS). UV-Visible absorption spectroscopy (Cary 5000 UV-Vis-NIR, Agilent) was used to identify the as-synthesized particles in solution, based on surface plasmon resonance. Fourier Transform Infra-Red (FTIR) spectrometry (Vertex 70, Bruker) was used in ATR mode (resolution of 2 cm^{-1}) to identify the chemical structures of the samples.

3.3- Results

3.3.1- Electrical characterization

The electrical characteristics (voltage and current) of a typical discharge generated at 22 kV voltage amplitude and 500 ns pulse width are shown in Figure 42a. Based on the current profile, the displacement current (due to voltage rise) has a peak ~10 A, and the discharge current is ~25 A. In the illustrated example, the discharge starts at ~220 ns, then the current rapidly increases to ~25 A. At the same time, the voltage drops from ~22 to ~8 kV. The injected charge (Q) and energy (E) of the discharge are calculated (by integrating the current and power over time, respectively) to be ~6 µC and 54 mJ, respectively. Notably, the occurrence of successful discharge and the moment of breakdown are randomly determined; however, the latter significantly depends on pulse width. Therefore, the values of Q and E values may significantly change. After 30 minutes of discharge at 10 Hz, both liquids change color (Figure 42b), which indicates that they contain nanoparticles. Moreover, jelly-like matter accumulates at the interface of the two liquids. To identify the nature of the produced nanoparticles and the accumulated matter, the materials were analyzed by TEM, as discussed in subsequent sections.

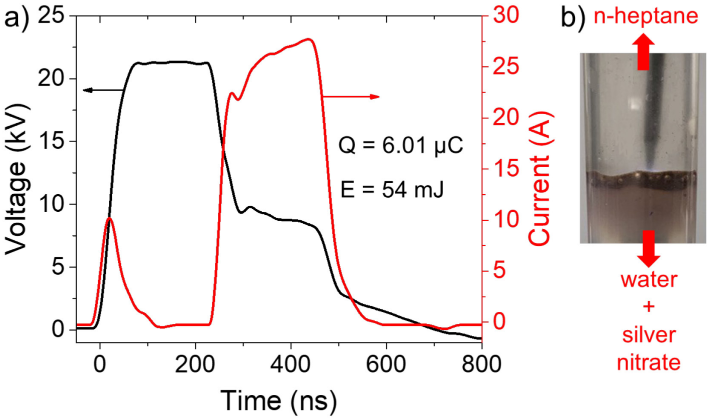

Figure 42. – a) Electrical characteristics (current and voltage) of a typical discharge generated at the voltage amplitude of 22 kV and the pulse width of 500 ns. b) Electrode-liquid configuration.

3.3.2- Characterization of the solution

After discharge, the liquids were characterized by FTIR and UV-Vis spectroscopy. Figure 43 shows the FTIR spectra of unprocessed and processed liquid heptane, as well as the spectrum of solid matter (after evaporation of the liquid heptane at room temperature). Considering that the FTIR spectra of the liquid before and after treatment are similar to that of water and show no appreciable differences, they are not presented in Figure 43.

Despite the change in the color of heptane liquid after processing, the difference between the spectra of processed and unprocessed heptane is insignificant (Figure 43). This is probably due to the low concentration of particles in heptane. However, the FTIR spectrum of solid matter is quite different from that of heptane, and it exhibits unique characteristics. In the range of 2800–3100 cm^{-1} (Figure 43a), all spectra present absorbance peaks at 2856, 2874, 2924, and 2958 cm^{-1}, corresponding to the stretching vibrations of -CH_2- (symmetric), -CH_3 (symmetric), -CH_2- (asymmetric), and -CH_3 (asymmetric), respectively [133]. The spectral peaks of processed and unprocessed heptane are perfectly superimposed; however, those of the analyzed solid matter exhibit different intensities. Clearly, the intensity ratio of the -CH_3 peaks to the -CH_2 peaks in the spectrum of solid matter is much less than that measured for processed or unprocessed heptane. This indicates that the process of matter formation produces a hydrocarbon network with fewer pendant CH_3 groups.

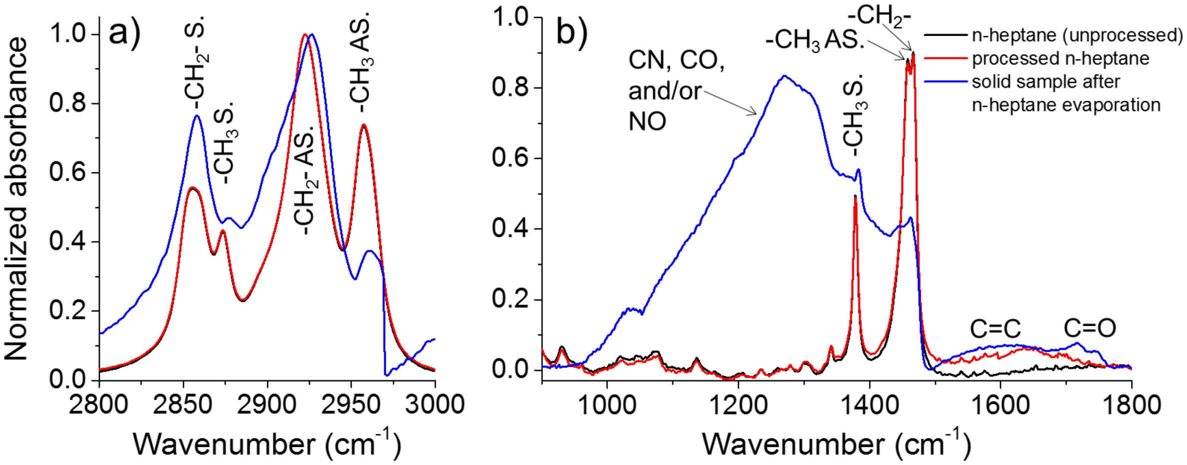

Figure 43. – FTIR spectra of unprocessed heptane, processed heptane, and the solid sample after liquid evaporation (S. for symmetric and AS. for asymmetric) in the range of a) 2800–3000 and b) 900–1800 cm^{-1}. Discharge conditions: 22 kV voltage amplitude, 500 ns pulse width, 10 Hz frequency, and 30 min processing time.

In the spectra of heptane (processed and unprocessed), the absorbance peaks corresponding to -CH_3 symmetric bending, -CH_3 asymmetric bending, -CH_2- bending, and C-H out-of-plane bending are detected at ~1378, 1455, 1470, and 720–790 cm^{-1}, respectively [138,139] (Figure 43b). However, in the range of 900–1500 cm^{-1}, the spectrum of solid matter exhibits one broad peak at ~1050–1350 cm^{-1} that may be related to CN, CO, and/or NO groups [140,141]. These groups are probably formed via the reaction of carbonaceous compounds with silver nitrate and/or via the incorporation of N_2 and O_2 in the structure after liquid evaporation in air. Moreover, unlike the spectra of processed and unprocessed heptane, the spectrum of solid matter shows peaks at ~1751–1770 and 1633 cm^{-1}, corresponding to C=O and C=C groups, respectively [142, 143].

The solutions of as synthesized particles were analyzed by UV-Vis absorption spectroscopy. Figure 44 compares the spectra of processed silver nitrate and processed heptane, and it shows that the former exhibits a broad peak near 400 nm (Figure 44a), similar to the plasmonic peak of silver particles [144]. Comparatively, the spectrum of processed heptane (Figure 44b) shows several peaks at ~213, 252, 260, and 329 nm that are usually attributed to carbonaceous nanomaterials, such as fullerene-60 (C_{60}), graphite, and graphite oxide [145-149]. Further characterizations are needed to confirm the carbon structure in the sample.

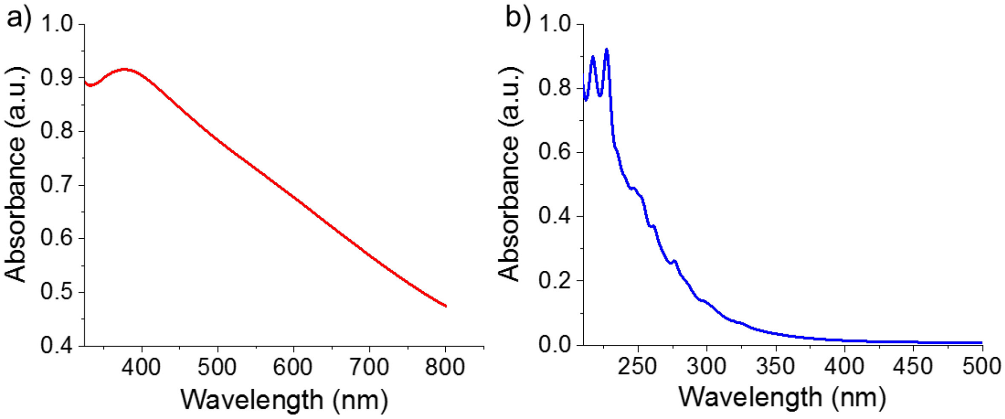

Figure 44. – UV-Vis spectra spectra of a) processed silver nitrate and b) processed heptane. Discharge conditions: 22 kV voltage amplitude, 500 ns pulse width, 10 Hz frequency, and 30 min processing time

3.4- TEM characterization

To further characterize the synthesized material, droplets taken from heptane and from the aqueous solution after processing were dropcasted onto TEM grids and analyzed using TEM microscopy. Figures 45a and 45b present low- and high-resolution TEM images of the particles formed in heptane, respectively. The image in Figure 45b (intermediate resolution) demonstrates that these particles exhibit a broad size distribution, with sizes less than 100 nm. Moreover, the EDS spectrum (eds 1) of the sample is dominated by C and Ag signals, and the two peaks exhibit similar intensities. Considering that the particles in the imaged zone are located in a TEM hole, the C signal is definitely attributed to the produced material and not to the TEM carbon film. Figure 45c shows the image of a single particle (diameter ~80 nm) surrounded by a carbon matrix in which fine particles are embedded. EDS analysis of the red-encircled zone in Figure 45c (eds 2) demonstrates that the analyzed region is primarily composed of Ag and C elements; however, the intensity of the C peak is almost twice as high as that of the Ag peak. Finally, the high-resolution TEM image in Figure 45d shows that the Ag atoms in the synthesized material are arranged in a crystal structure, and that the interplanar distance of the crystalline arrangement coincides with that of the Ag (111) plane [150].

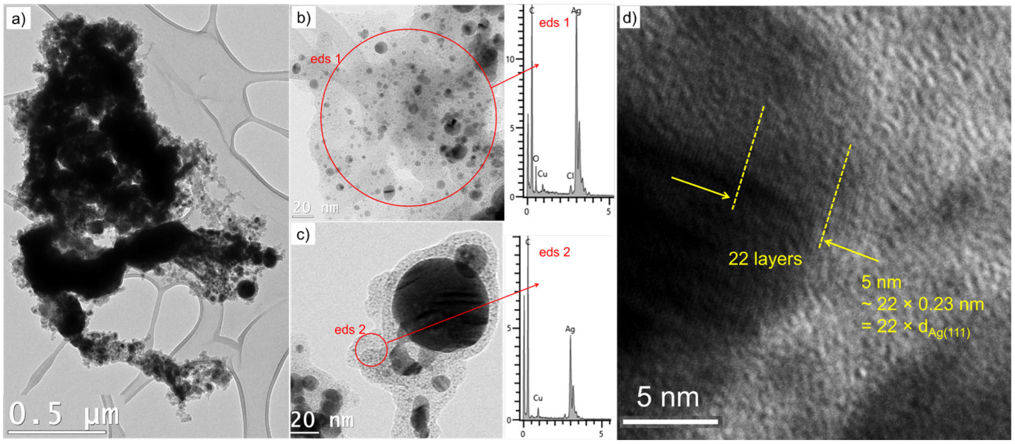

Figure 45. – a) Low- and b) intermediate-resolution TEM images of the material collected from heptane after discharge. c) Intermediate0resolution TEM image of individual Ag particles surrounded by a hydrocarbon network. d) High-resolution TEM image showing the crystalline nature of an Ag particle. Discharge conditions: 22 kV voltage amplitude, 500 ns pulse width, 10 Hz frequency, and 30 min processing time.

Further statistical analysis of particle size was performed, and the histogram depicted in Figure 46 (performed on the TEM image in the inset) shows that most particles are embedded in a carbon matrix and have diameters less than 5 nm. The large particles are less numerous. The data is nicely fitted by a lognormal distribution with a mean size and standard deviation of 4.5 and 5.7 nm, respectively.

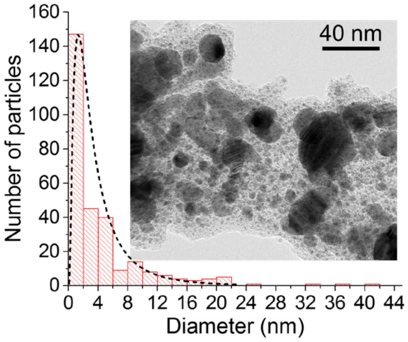

Figure 46. – Histogram (statistical analysis performed on the figure in the inset) showing the size distribution of the particles produced in heptane. Discharge conditions: 22 kV voltage amplitude, 500 ns pulse width, 10 Hz frequency, and 30 min processing time.

The TEM image of particles collected from aqueous solution (Figure 47a) shows that these particles are carbon free. In addition to the Ag signal, a C signal is detected in the EDS spectrum of the sample, and it is attributed to the carbon layer of the TEM grid. Statistical analysis of the particle size demonstrates that most particles have diameters in the range of 5–20 nm, but the a few ones are up to 140-nm large (Figure 47b).

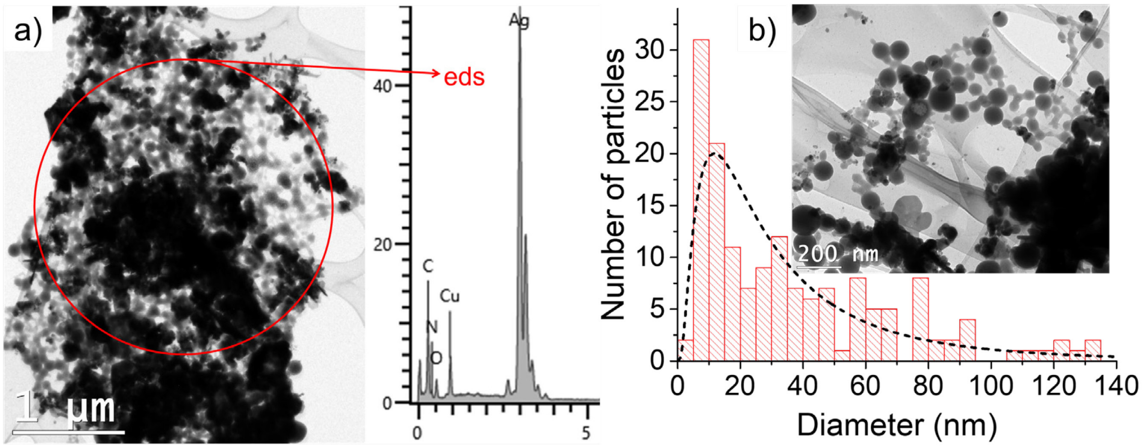

Figure 47. – a) Low-resolution TEM image of the material collected from the aqueous solution. b) Histogram (statistical analysis) showing the size distribution of particles: mean = 37.4 nm and standard deviation = 31.1 nm. Discharge conditions: 22 kV voltage amplitude, 500 ns pulse width, 10 Hz frequency, and 30 min processing time

3.5- Characterization of particles synthesized at shorter pulse width

To assess the effect of plasma lifetime on the size and composition of the products, we characterized the particles synthesized under the effect of 100 ns discharges. Based on the current waveform shown in Figure 48a, the current peak of a typical discharge generated at short pulse width (100 ns) is similar to that of the 500 ns discharge; however, the current flow period is relatively shorter (~150 ns vs. ~300 ns). Although the period of current flow may be considered as the lifetime of discharge, spark discharges in liquid last a bit longer than this period [151] (see discussion 3.6). The UV-Vis spectra shown in Figure 49b demonstrate that the particles synthesized in heptane by 100 ns discharges are similar to those produced by 500 ns discharges. However, the FTIR spectra of the two sets of particles present significant differences in the ranges of 1000–1500 (Figure 48c) and 2800–3000 cm^{-1} (Figure 48d). In particular, the -CH_3 symmetric vibration peak detected at 2874 cm^{-1} disappears upon switching to shorter pulse width, as does the peak at 2958 cm^{-1} (-CH_3 asymmetric vibration). The peak at 2924 cm^{-1} (-CH_2- asymmetric) is not significantly affected by the pulse width of the discharge. Overall, these results indicate that pulse width slightly affects the carbonaceous composition of particles synthesized in heptane.

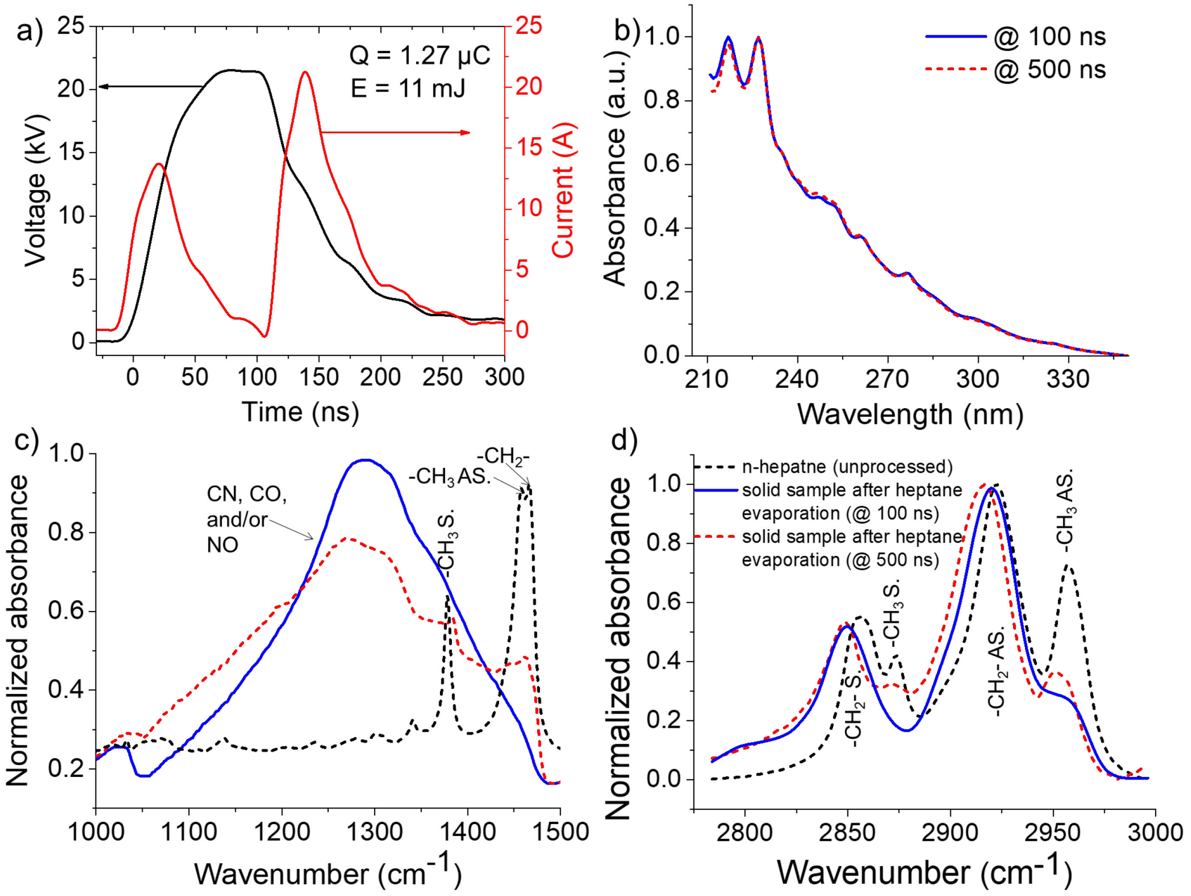

Figure 48. – a) Electrical characteristics of a typical discharge generated at 100 ns pulse width. b) UV-Vis spectra of materials synthesized in heptane at 100 and 500 ns pulse width. c) and d) FTIR spectra of unprocessed heptane and the solid particles generated in heptane (after heptane evaporation) at 100 and 500 ns pulse widths.

Low-resolution TEM analysis shows that the particles synthesized in heptane using 100 ns discharge exhibit a film-like morphology with nanoparticle agglomerations on the film surface (Figure 49a). The EDS spectra of the red encircled zones (insets of Figure 49a) present Ag and C signals. In zone 1 (agglomeration of particles), the intensities of the Ag and C peaks are comparable; however, in zone 2 (film-like), the intensity of C is much higher than that of Ag. Statistical analysis demonstrates that most particles in the agglomeration have diameters between 10 and 20 nm, and some of them are as large as 45 nm (Figure 49b). A magnified image of the film-like structure (Figure 49c) shows that the particles on it have similar sizes and are almost homogeneously distributed. The size distribution of these particles is actually 1–7 nm, and the average size is 4 nm (Figure 50d). In addition to particles, the TEM image shows some individual-sheet-like material (Figure 49e). EDS analyses of the local regions on this material demonstrate that it is primarily composed of carbon, with some Ag. High-resolution TEM analysis (yellow delimited zone) shows that the sheet-like material is ultrathin (probably a monolayer), and it contains fine nanoparticles (Figure 49f). The high contrast of the edge is apparently a consequence of wrapping phenomenon, referred to as ‘wrapped sheet’ in Figure 49f.

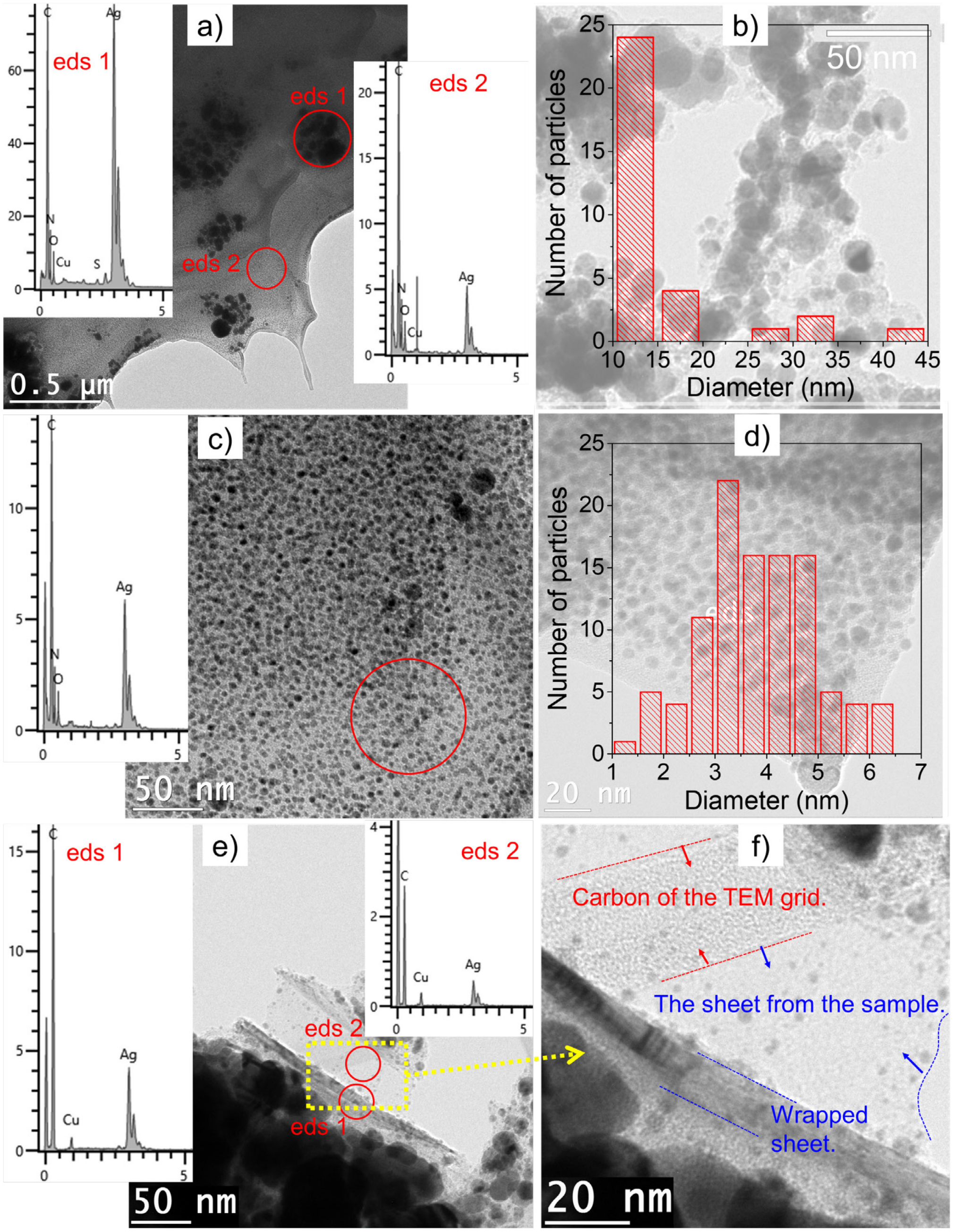

Figure 49. – a) TEM image of the material collected from heptane. b) Histogram (statistical analysis) showing the size distribution of the agglomerated particles. c) High-resolution TEM image showing the composition of the film-like material. d) Histogram (statistical analysis) showing the size distribution of fine particles in the film-like material. e) and f) Images of the individual-sheet-like material. Discharge conditions: 22 kV voltage amplitude, 100 ns pulse width, 10 Hz frequency, and 30 min processing time.

As for the particles collected from the aqueous solution, their morphological characteristics and size distribution are similar to those of the corresponding particles produced at 500 ns pulse width (typical TEM image shown in Figure 50a). Most particles have diameters in the range of 5–20 nm, and some are as large as 70 nm.

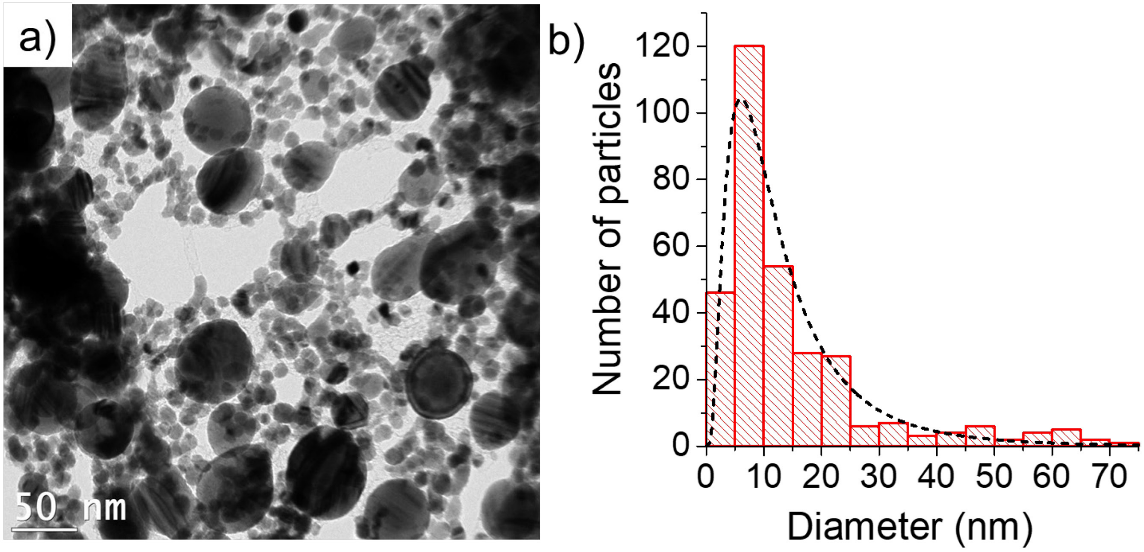

Figure 50. – a) TEM image of the material collected from the aqueous solution. b) Histogram (statistical analysis performed on a)) showing the size distribution of particles: mean = 14.5 nm and standard deviation = 13.6 nm. Discharge conditions: 22 kV voltage amplitude, 100 ns pulse width, 10 Hz frequency, and 30 min processing time.

3.6- Discussion

Spark discharges in liquid are known to produce plasmas with non-conventional properties such as high density of species (10^{17}–10^{19} cm^{-3}), high temperature (5000–10000 K), high pressure (tens of bar), and short lifetime [125,152]. Similarly, the spatial and temporal gradients of these properties are unconventionally strong. The former is attributed to the confinement of the plasma in a liquid that is usually at room temperature and atmospheric pressure. Meanwhile, the latter is due to the short lifetime of the plasma (nanosecond time scale). Despite its short lifetime, the emission generated by discharges in liquid lasts beyond the voltage pulse, and in some cases, bubbles are formed in the medium [153]. Under these conditions, the plasma exhibits strong chemical and physical interactions with the electrodes (through reaction with highly reactive species and bombardment by energetic species, respectively), as well as with the surrounding liquid. Considering that both, electrode erosion and liquid decomposition contribute to the formation of nanomaterials, the nature of these materials can be predefined by selecting the appropriate electrodes and liquid.

Particles produced by spark discharges in liquid often exhibit two size distributions. The small particles (< 10 nm) are supposedly produced in the plasma core, whereas the larger ones (< 1 µm) are ejected from the electrode surface after it is hit by the plasma. Previously, the feasibility of nanomaterial synthesis by sustaining discharges at the interface of two liquids has been demonstrated for at least two discharge modes. In the case of streamer discharges sustained at the interface of two dielectric liquids, carbon-based [130] and hydrogenated SiOC nanoparticles [129] had been synthesized at the interface of water-heptane and water-hexamethyldisilazane ($(CH_3)_3Si\text{-}NH\text{-}Si(CH_3)_3$), respectively. Meanwhile, in the case of spark/arc discharges sustained in two-liquid microemulsions, Fe nanoparticles had been produced by erosion of two Fe electrodes immersed in a microemulsion of water and toluene [136]. In this study, we explore a novel discharge configuration wherein the spark discharges are sustained between a carbon electrode (the anode) immersed in liquid heptane and aqueous silver nitrate solution (the cathode). The synthesis of nanoparticles using this configuration is thus due to the reduction of Ag ions by the spark discharge in liquid heptane, which means that the plasma-solution interaction is key in the process of nanomaterial production.

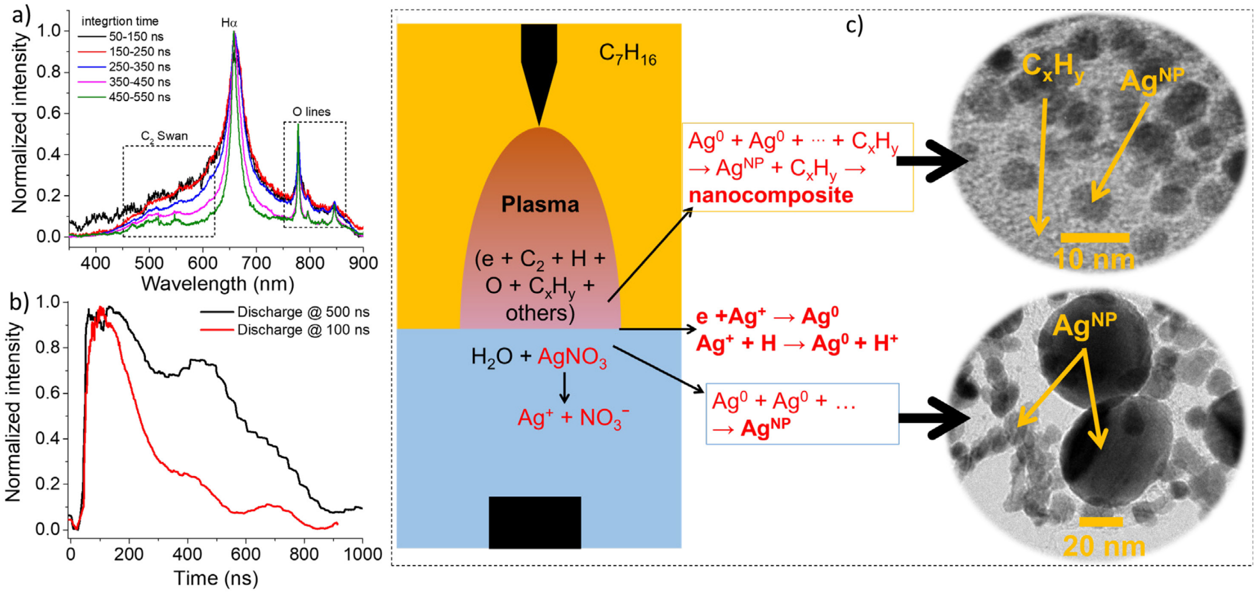

Figure 51. – a) Temporal evolution of the optical emission spectra recorded for discharges generated at 22 kV and 500 ns. b) PM signals acquired for discharges generated at 100 and 500 ns pulse widths. c) Descriptive scheme showing the main reactions implicated in the synthesis of material in heptane and in the solution.

To elucidate the mechanism of nanomaterial synthesis, it is important to consider the plasma composition. This latter (produced at 500 ns pulse width) was analyzed using optical emission spectroscopy. Figure 51a presents the temporal evolution (within the pulse width) of the normalized spectra (each spectrum was integrated during 100 ns). The lines in the spectra represent C_2 Swan bands (Δv = 1: ~468–475 nm, Δv = 0: ~506–517 nm, Δv = -1: ~545–565 nm), Hα (656.3 nm), and O (777–844 nm). Surprisingly, Ag lines are not detected. Note that the broadness of the Hα line is due to the high electron density in the plasma (not quantified here, but the values estimated under similar conditions are provided in [128]). As for the emission lifetime, it was estimated using a PM tube, and Figure 51b shows the signals acquired for 100 and 500 ns discharges. As expected, higher pulse widths extend the lifetime of the plasma, and the lifetime is longer than the pulse width (due to post-discharge phase), irrespective of its value.

When a plasma is coupled with water, numerous reactive species (O, OH, H_2O_2, etc.) are produced [154], some of which have long lifetimes [155]. Herein, the reactive species present at the plasma-solution interface interact with Ag ions (Ag^+) to form Ag^0. As emission peaks of Ag were not detected, it seems that there are no Ag atoms in the discharge region. This unexpected finding may be due to the high electron numbers available at the plasma-solution interface that simultaneously reduce many Ag ions to Ag^0; the main reactions reported in similar systems are $Ag^+ + e \rightarrow Ag^0$ (R1) and $Ag^+ + H \rightarrow Ag^0 + H+$ (R2) [99]. Considering that the electrons are concentrated in a small region (the plasma-solution interface is around 100 μm^2), the density of reduced atoms is relatively high, and so, the Ag nanoparticles are formed rapidly. Since the particles collected from the solution side are carbon free and larger than those collected from heptane, it is expected that these particles are formed at the interface (via R1 and R2) and/or in solution (via solvated electrons and other reactive species). The particles collected from heptane are quite different from those in the solution. Indeed, these particles exhibit two size distributions, < 10 nm (majority) and > 10 nm (minority), and carbon is detected in both. We believe that the fine particles embedded in a hydrocarbon network are grown in the plasma core where C_2 Swan bands are detected. The formation of the hydrocarbon network in the core impedes the growth of Ag nanoparticles, and so, the particles remain small (< 10 nm). Meanwhile, the large particles in heptane are supposedly formed during a discharge at the heptane-solution interface, and during subsequent discharges, these particles are ejected from the solution towards heptane, where they embed in a hydrocarbon network.

3.7- Summary

In this chapter (which is a part of a paper), we investigate the Ag nanoparticles produced by spark discharge in an immiscible mixture of heptane and aqueous silver nitrate solution. The discharges are generated in heptane that is in contact with the solution. At 22 kV voltage amplitude and 500 ns pulse width, particles are produced in both liquids. The material collected from heptane is a nanocomposite material, i.e. Ag nanoparticles (< 10 nm) in a hydrocarbon network. However, the particles in aqueous solution are carbon-free Ag nanoparticles (10–150 nm). To assess the effect of discharge lifetime on the synthesized materials, discharges were run at shorter pulse width (100 ns). The results show that the particles produced under this condition are similar to those generated at 500 ns, but their size distribution is smaller. Overall, the data indicate that the novel spark discharge in liquid technique proposed herein produces nanomaterials by plasma-induced ion reduction. The originality of this discharge is related to its non-conventional properties of pressure, density, and temperature, and based on these properties, it may be used to synthesize nanoalloys.

Conclusion

The main objective of this work was to develop a simplified method to produce nanoparticles. Regarding this purpose, we proposed almost novel plasma liquid systems in which spark discharge in a hydrocarbon liquid in contact with an aqueous solution was used to produced nanoparticles.

Looking at the literature illustrated that most of the plasma liquid systems that have been studied were related to the plasma in-liquid or over liquid systems, and only a few of them investigated plasma in multiple liquid systems. Although even in multiple plasma liquid systems studies most usually just have been emphasised on the morphology and dynamics of the plasma rather than paid attention to the ability of these systems to forming different nanomaterial.

Therefore, here we were focused on producing Ag nanoparticles using discharges in two immiscible liquid systems. Different material characterization techniques, like transmission electron microscopy, x-ray diffraction analysis (not showed here), UV-Vis spectroscopy, etc., were used in order to fully understand of produced nanomaterials' characteristics. Furthermore, optical emission spectroscopy and photomultiplier techniques were applied to illustrate the characteristics of the discharge occurring during nanomaterial synthesis.

Spark discharges in heptane in-contact with silver nitrate solution produced induced a colour change of both liquids and lead to the formation of nanoparticles. Most particles collected from heptane are nanocomposites of Ag nanoparticles (<10 nm) in a hydrocarbon network. Meanwhile, the material collected from the silver nitrate solution is Ag nanoparticles (10–150 nm of diameter). Shortening the high voltage pulse width from 500 to 100 ns, the discharges generate similar materials in both liquids; however, the size distribution of these materials is relatively smaller.

At this stage, it seems that the main route of synthesis is through plasma-induced ion reduction. The uniqueness of this in-liquid spark discharge is due to its high density, instantaneous pressure, and temperature, which increases the synthesis yield significantly.

References

[1] Malhotra, B.D. and Ali, M.A., 2018. Nanomaterials in biosensors: fundamentals and applications. Nanomaterials for Biosensors, p.1.

[2] Sekhon, B.S., 2010. Food nanotechnology–an overview. Nanotechnology, science and applications, 3, p.1.

[3] Pandiyan, G.K. and Prabaharan, T., 2020. Implementation of nanotechnology in fuel cells. Materials Today: Proceedings, 33, pp.2681-2685.

[4] Banin, U., Waiskopf, N., Hammarström, L., Boschloo, G., Freitag, M., Johansson, E.M., Sá, J., Tian, H., Johnston, M.B., Herz, L.M. and Milot, R.L., 2020. Nanotechnology for catalysis and solar energy conversion. Nanotechnology, 32(4), p.042003.

[5] Kunduru, K.R., Nazarkovsky, M., Farah, S., Pawar, R.P., Basu, A. and Domb, A.J., 2017. Nanotechnology for water purification: applications of nanotechnology methods in wastewater treatment. Water purification, pp.33-74.

[6] Iravani, S., Korbekandi, H., Mirmohammadi, S.V. and Zolfaghari, B., 2014. Synthesis of silver nanoparticles: chemical, physical and biological methods. Research in pharmaceutical sciences, 9(6), p.385.

[7] Rane, A.V., Kanny, K., Abitha, V.K. and Thomas, S., 2018. Methods for synthesis of nanoparticles and fabrication of nanocomposites. In Synthesis of inorganic nanomaterials (pp. 121-139). Woodhead Publishing (book chapter)

[8] Hwang, N.M. and Lee, D.K., 2010. Charged nanoparticles in thin film and nanostructure growth by chemical vapour deposition. Journal of Physics D: Applied Physics, 43(48), p.483001.

[9] Izadi, A., 2020. Plasma Application for Synthesis of Novel Nanostructures and Mechanical Properties Investigation. Michigan State University (thesis).

[10] Tsai, C.Y., Hsi, H.C., Kuo, T.H., Chang, Y.M. and Liou, J.H., 2013. Preparation of Cu-doped TiO2 photocatalyst with thermal plasma torch for low-concentration mercury removal. Aerosol and Air Quality Research, 13(2), pp.639-648.

[11] Seo, J.H. and Hong, B.G., 2012. Thermal plasma synthesis of nano-sized powders. Nuclear engineering and technology, 44(1), pp.9-20.

[12] Hu, C., Shen, J.J., Chang, A.L. and Wei, T.C., 2019. Microwave plasma torch synthesis of ZnAl oxides as adsorbent and photocatalyst for organic compounds removal. Powder Technology, 344, pp.454-462.

[13] Feng, T., Wang, Q. and Khan, W.Q., 2018. Synthesis of carbon-encapsulated Iron and iron nitride nanoparticles from ferrocene through reactive radio-frequency thermal plasma. Journal of nanoscience and nanotechnology, 18(10), pp.7078-7084.

[14] Mohai, I., Gál, L., Szépvölgyi, J., Gubicza, J. and Farkas, Z., 2007. Synthesis of nanosized zinc ferrites from liquid precursors in RF thermal plasma reactor. Journal of the European Ceramic Society, 27(2-3), pp.941-945.

[15] Mavier, F., Rat, V., Bienia, M., Lejeune, M. and Coudert, J.F., 2017. Suspension and precursor solution plasma spraying by means of synchronous injection in a pulsed arc plasma. Surface and Coatings Technology, 318, pp.18-27.

[16] Schuffenhauer, C., Parkinson, B.A., Jin-Phillipp, N.Y., Joly-Pottuz, L., Martin, J.M., Popovitz-Biro, R. and Tenne, R., 2005. Synthesis of Fullerene-Like Tantalum Disulfide Nanoparticles by a Gas-Phase Reaction and Laser Ablation. Small, 1(11), pp.1100-1109.

[17] Wang, Z., Liu, Y. and Zeng, X., 2006. One-step synthesis of γ-Fe2O3 nanoparticles by laser ablation. Powder technology, 161(1), pp.65-68.

[18] Hartanto, A.B., Ning, X., Nakata, Y. and Okada, T., 2004. Growth mechanism of ZnO nanorods from nanoparticles formed in a laser ablation plume. Applied Physics A, 78(3), pp.299-301.

[19] Amendola, V. and Meneghetti, M., 2009. Laser ablation synthesis in solution and size manipulation of noble metal nanoparticles. Physical chemistry chemical physics, 11(20), pp.3805-3821.

[20] Kazakevich, P.V., Simakin, A.V., Voronov, V.V. and Shafeev, G.A., 2006. Laser induced synthesis of nanoparticles in liquids. Applied Surface Science, 252(13), pp.4373-4380.

[21] Kumar, B. and Thareja, R.K., 2010. Synthesis of nanoparticles in laser ablation of aluminum in liquid. Journal of applied physics, 108(6), p.064906.

[22] Gondal, M.A., Drmosh, Q.A., Yamani, Z.H. and Saleh, T.A., 2009. Synthesis of ZnO2 nanoparticles by laser ablation in liquid and their annealing transformation into ZnO nanoparticles. Applied surface science, 256(1), pp.298-304.

[23] Renze, Y.U., Zhaoyuan, L.I.U., Jiao, L.I.N., Xinyi, H.E., Linsheng, L.I.U., Xiong, Q., Qiang, C.H.E.N. and Ostrikov, K.K., 2021. Colorimetric quantification of aqueous hydrogen peroxide in the DC plasma-liquid system. Plasma Science and Technology, 23(5), p.055504.

[24] Richmonds, C. and Sankaran, R.M., 2008. Plasma-liquid electrochemistry: Rapid synthesis of colloidal metal nanoparticles by microplasma reduction of aqueous cations. Applied Physics Letters, 93(13), p.131501.

[25] Burakov, V.S., Kiris, V.V., Nedelko, M.I., Tarasenka, N.N., Nevar, A.A. and Tarasenko, N.V., 2017. Atmospheric pressure plasma in contact with liquid and its application for nanoparticles synthesis. The European Physical Journal Applied Physics, 79(1), p.10801.

[26] Kaneko, T., Chen, Q., Harada, T., & Hatakeyama, R. (2011). Structural and reactive kinetics in gas–liquid interfacial plasmas. Plasma Sources Science and Technology, 20(3), 034014..

[27] Pawlat, J., Hensel, K. and Ihara, S., 2005. Decomposition of humic acid and methylene blue by electric discharge in foam. Acta Physica Slovaca, 55(5), pp.479-485.

[28] Pawłat, J., Hensel, K. and Ihara, S., 2006. Generation of oxidants and removal of indigo blue by pulsed power in bubbling and foaming systems. Czechoslovak Journal of Physics, 56(2), pp.B1174-B1178.

[29] Feynman, R.P., 1960. There's Plenty of Room at the Bottom. Caltech Engineering & Science. Retrieved, Feb. 14, 2014.

[30] Mansoori, G.A., 2005. Principles of nanotechnology: molecular-based study of condensed matter in small systems. World Scientific (book chapter).

[31] Santamaria, A., 2012. Historical overview of nanotechnology and nanotoxicology. Nanotoxicity, pp.1-12

[32] Komanduri, R., Lucca, D.A. and Tani, Y., 1997. Technological advances in fine abrasive processes. CIRP Annals, 46(2), pp.545-596.

[33] Jeevanandam, J., Barhoum, A., Chan, Y.S., Dufresne, A. and Danquah, M.K., 2018. Review on nanoparticles and nanostructured materials: history, sources, toxicity and regulations. Beilstein journal of nanotechnology, 9(1), pp.1050-1074.

[34] Pareek, V., Bhargava, A., Gupta, R., Jain, N. and Panwar, J., 2017. Synthesis and applications of noble metal nanoparticles: a review. Advanced Science, Engineering and Medicine, 9(7), pp.527-544.

[35] Parashar, M., Shukla, V.K. and Singh, R., 2020. Metal oxides nanoparticles via sol–gel method: a review on synthesis, characterization and applications. Journal of Materials Science: Materials in Electronics, 31(5), pp.3729-3749.

[36] Pengo, P., Baltzer, L., Pasquato, L. and Scrimin, P., 2007. Substrate modulation of the activity of an artificial nanoesterase made of peptide-functionalized gold nanoparticles. Angewandte Chemie, 119(3), pp.404-408.

[37] Holthausen, D., Vasani, R.B., McInnes, S.J., Ellis, A.V. and Voelcker, N.H., 2012. Polymerization-amplified optical DNA detection on porous silicon templates. ACS Macro Letters, 1(7), pp.919-921.

[38] Chen, S., Yuan, R., Chai, Y. and Hu, F., 2013. Electrochemical sensing of hydrogen peroxide using metal nanoparticles: a review. Microchimica Acta, 180(1), pp.15-32.

[39] De Volder, M.F., Tawfick, S.H., Baughman, R.H. and Hart, A.J., 2013. Carbon nanotubes: present and future commercial applications. science, 339(6119), pp.535-539.

[40] Salata, O.V., 2004. Applications of nanoparticles in biology and medicine. Journal of nanobiotechnology, 2(1), pp.1-6.

[41] Jordan, C.C., Kaiser, I. and Moore, V.C., 2014. 2013 nanotechnology patent literature review: Graphitic carbon-based nanotechnology and energy applications are on the rise. Nanotech. L. & Bus., 11, p.111.

[42] Cheng, H., Ma, J., Zhao, Z. and Qi, L., 1995. Hydrothermal preparation of uniform nanosize rutile and anatase particles. Chemistry of Materials, 7(4), pp.663-671.

[43] Cao, Y., Yang, W., Zhang, W., Liu, G. and Yue, P., 2004. Improved photocatalytic activity of Sn 4+ doped TiO 2 nanoparticulate films prepared by plasma-enhanced chemical vapor deposition. New Journal of Chemistry, 28(2), pp.218-222.

[44] Khanna, P., Kaur, A. and Goyal, D., 2019. Algae-based metallic nanoparticles: Synthesis, characterization and applications. Journal of microbiological methods, 163, p.105656.

[45] Das, D. and Roy, A., 2020. Synthesis of diameter controlled multiwall carbon nanotubes by microwave plasma-CVD on low-temperature and chemically processed Fe nanoparticle catalysts. Applied Surface Science, 515, p.146043.

[46] Bogaerts, A., Neyts, E., Gijbels, R. and Van der Mullen, J., 2002. Gas discharge plasmas and their applications. Spectrochimica Acta Part B: Atomic Spectroscopy, 57(4), pp.609-658.

[47] Dave, H., Ledwani, L. and Nema, S.K., 2019. Nonthermal plasma: a promising green technology to improve environmental performance of textile industries. In The Impact and Prospects of Green Chemistry for Textile Technology (pp. 199-249). Woodhead Publishing (book chapter).

[48] Kogelschatz, U., 2002. Filamentary, patterned, and diffuse barrier discharges. IEEE Transactions on plasma science, 30(4), pp.1400-1408.

[49] Levasseur, O., Profili, J., Gangwar, R. K., Naudé, N., Clergereaux, R., Gherardi, N., & Stafford, L. (2014). Experimental and modelling study of organization phenomena in dielectric barrier discharges with structurally inhomogeneous wood substrates. Plasma Sources Science and Technology, 23(5), 054006.

[50] Nadal, E., Milaniak, N., Glenat, H., Laroche, G. and Massines, F., 2021. A new approach for synthesizing plasmonic polymer nanocomposite thin films by combining a gold salt aerosol and an atmospheric pressure low-temperature plasma. Nanotechnology, 32(17), p.175601.

[51] Matouk, Z., Torriss, B., Rincón, R., Mirzaei, A., Margot, J. and Chaker, M., 2021. Atmospheric plasma dielectric barrier discharge: A simple route to produce superhydrophilic TiO2@ carbon nanostructure. Plasma Processes and Polymers, 18(3), p.2000173.

[52] Abubakirov, E.B., Afanas’ev, V.P., Agarwal, A., Agarwal, S.K., Agiral, A., Akatsuka, H., Akino, N., Akishev, Y.S., Akiyama, H., Aksenov, I.I. and Aksyonov, D.S., 2009. 2009 Index IEEE Transactions on Plasma Science Vol. 37. IEEE Transactions on Plasma Science, 37(12), p.2403.

[53] Bapat, A., Anderson, C., Perrey, C.R., Carter, C.B., Campbell, S.A. and Kortshagen, U., 2004. Plasma synthesis of single-crystal silicon nanoparticles for novel electronic device applications. Plasma physics and controlled fusion, 46(12B), p.B97.

[54] Oh, J.W., Na, H., Cho, Y.S. and Choi, H., 2018. In situ synthesis of bimetallic tungsten-copper nanoparticles via reactive radio-frequency (RF) thermal plasma. Nanoscale research letters, 13(1), pp.1-7.

[55] Na, H., Park, J.W., Choi, H. and Cho, Y.S., 2020. Radio frequency thermal plasma-processed Ni-W nanostructures for printable microcircuit electrodes. Materials & Design, 191, p.108590.

[56] Shimizu, Y., Kawaguchi, K., Sasaki, T. and Koshizaki, N., 2009. Generation of room-temperature atmospheric H 2/Ar microplasma jet driven with pulse-modulated ultrahigh frequency and its application to gold nanoparticle preparation. Applied Physics Letters, 94(19), p.191504.

[57] Vollath, D. and Sickafus, K.E., 1992. Synthesis of nanosized ceramic oxide powders by microwave plasma reactions. Nanostructured Materials, 1(5), pp.427-437.

[58] Chau, J.L.H., Hsu, M.K. and Kao, C.C., 2006. Microwave plasma synthesis of Co and SiC-coated Co nanopowders. Materials Letters, 60(7), pp.947-951.

[59] David, B., Pizurova, N., Schneeweiss, O., Bezdička, P., Morjan, I. and Alexandrescu, R., 2005. Iron/graphite core-shell structured nanoparticles prepared by annealing of nanopowder. In Materials Science Forum (Vol. 480, pp. 469-476). Trans Tech Publications Ltd.

[60] Alexandrescu, R., Morjan, I., Dumitrache, F., Scarisoreanu, M., Soare, I., Fleaca, C., Birjega, R., Popovici, E., Gavrila, L., Prodan, G. and Ciupina, V., 2008. Photochemistry aspects of the laser pyrolysis addressing the preparation of oxide semiconductor photocatalysts. International Journal of Photoenergy, 2008.

[61] Puretzky, A.A., Geohegan, D.B., Fan, X. and Pennycook, S.J., 2000. Dynamics of single-wall carbon nanotube synthesis by laser vaporization. Applied Physics A, 70(2), pp.153-160.

[62] Vollath, D., 2008. Plasma synthesis of nanopowders. Journal of Nanoparticle Research, 10(1), pp.39-57.

[63] Xu, X., Duan, G., Li, Y., Liu, G., Wang, J., Zhang, H., Dai, Z. and Cai, W., 2014. Fabrication of gold nanoparticles by laser ablation in liquid and their application for simultaneous

electrochemical detection of Cd2+, Pb2+, Cu2+, Hg2+. ACS applied materials & interfaces, 6(1), pp.65-71.

[64] Patil, P.P., Phase, D.M., Kulkarni, S.A., Ghaisas, S.V., Kulkarni, S.K., Kanetkar, S.M., Ogale, S.B. and Bhide, V.G., 1987. Pulsed-laser–induced reactive quenching at liquid-solid interface: Aqueous oxidation of iron. Physical review letters, 58(3), p.238.

[65] Dolgaev, S.I., Simakin, A.V., Voronov, V.V., Shafeev, G.A. and Bozon-Verduraz, F., 2002. Nanoparticles produced by laser ablation of solids in liquid environment. Applied surface science, 186(1-4), pp.546-551.

[66] Liang, C.H., Shimizu, Y., Sasaki, T. and Koshizaki, N., 2005. Preparation of ultrafine TiO 2 nanocrystals via pulsed-laser ablation of titanium metal in surfactant solution. Applied physics A, 80(4), pp.819-822.

[67] Musaev, O.R., Driver, M.S., Sutter, E.A., Caruso, A.N., Wrobel, J.M. and Kruger, M.B., 2013. Influence of the liquid environment on the products formed from the laser ablation of tin. Applied Physics A, 113(2), pp.355-359.

[68] Hickling, A. and Ingram, M.D., 1964. Contact glow-discharge electrolysis. Transactions of the Faraday Society, 60, pp.783-793.

[69] Martin, T.H., Williams, M. and Kristiansen, M. eds., 2013. JC Martin on pulsed power (Vol. 3). Springer Science & Business Media (book chapter).

[70] Napartovich, A.P., Akishev, Y.S., Deryugin, A.A., Kochetov, I.V., Pan'kin, M.V. and Trushkin, N.I., 1997. A numerical simulation of Trichel-pulse formation in a negative corona. Journal of Physics D: Applied Physics, 30(19), p.2726.

[71] Bonifaci, N., Denat, A., Atrazhev, V.M., Atrazhev, V.V., Kochetov, I.V. and Napartovich, A.P., 2002, July. Cathode sheath formation of corona discharge in liquid argon. In Proceedings of 2002 IEEE 14th International Conference on Dielectric Liquids. ICDL 2002 (Cat. No. 02CH37319) (pp. 131-134). IEEE.

[72] Li, Z., Bonifaci, N., Denat, A., Atrazhev, V.M. and Atrazhev, V.V., 2008. Ionization and charge transport phenomena in liquid helium induced by corona discharge. Journal of Electrostatics, 66(5-6), pp.263-274.

[73] Ollegott, K., Wirth, P., Oberste-Beulmann, C., Awakowicz, P. and Muhler, M., 2020. Fundamental Properties and Applications of Dielectric Barrier Discharges in Plasma-Catalytic Processes at Atmospheric Pressure. Chemie Ingenieur Technik, 92(10), pp.1542-1558.

[74] Ceccato, P., 2009. Filamentary plasma discharge inside water: initiation and propagation of a plasma in a dense medium (Doctoral dissertation, Ecole Polytechnique X).

[75] Belmonte, T., Hamdan, A., Kosior, F., Noël, C. and Henrion, G., 2014. Interaction of discharges with electrode surfaces in dielectric liquids: application to nanoparticle synthesis. Journal of Physics D: Applied Physics, 47(22), p.224016.

[76] Kuskova, N.I., 1983. Distribution mechanism of leaders in water. Sov. Phys.-Tech. Phys, 53, pp.924-5.

[77] Starikovskiy, A., Yang, Y., Cho, Y.I. and Fridman, A., 2011. Non-equilibrium plasma in liquid water: dynamics of generation and quenching. Plasma Sources Science and Technology, 20(2), p.024003.

[78] Sharbaugh, A.H., Devins, J.C. and Rzad, S.J., 1978. Progress in the field of electric breakdown in dielectric liquids. IEEE Transactions on Electrical Insulation, (4), pp.249-276.

[79] Lewis, T.J., 1998. A new model for the primary process of electrical breakdown in liquids. IEEE Transactions on Dielectrics and Electrical Insulation, 5(3), pp.306-315.

[80] Lewis, T.J., 2003. Breakdown initiating mechanisms at electrode interfaces in liquids. IEEE Transactions on Dielectrics and Electrical Insulation, 10(6), pp.948-955.

[81] Gubkin, J., 1887. Electrolytiche metallabscheidung an der freien oberflache einer salzosung. Ann. Phys. Chem. NF, 32, pp.114-115.

[82] Bruggeman, P. and Leys, C., 2009. Non-thermal plasmas in and in contact with liquids. Journal of Physics D: Applied Physics, 42(5), p.053001.

[83] Rezaei, F., Vanraes, P., Nikiforov, A., Morent, R. and De Geyter, N., 2019. Applications of plasma-liquid systems: A review. Materials, 12(17), p.2751.

[84] Yang, F., Li, Y., Liu, T., Xu, K., Zhang, L., Xu, C. and Gao, J., 2013. Plasma synthesis of Pd nanoparticles decorated-carbon nanotubes and its application in Suzuki reaction. Chemical engineering journal, 226, pp.52-58.

[85] Liu, T., Yang, F., Li, Y., Ren, L., Zhang, L., Xu, K., Wang, X., Xu, C. and Gao, J., 2014. Plasma synthesis of carbon nanotube-gold nanohybrids: efficient catalysts for green oxidation of silanes in water. Journal of Materials Chemistry A, 2(1), pp.245-250.

[86] Hayashi, Y., Machmudah, S., Takada, N., Kanda, H., Sasaki, K. and Goto, M., 2013. Decomposition of methyl orange using pulsed discharge plasma at atmospheric pressure: Effect of different electrodes. Japanese Journal of Applied Physics, 53(1), p.010212.

[87] Yan, T., Zhong, X., Rider, A.E., Lu, Y., Furman, S.A. and Ostrikov, K.K., 2014. Microplasma-chemical synthesis and tunable real-time plasmonic responses of alloyed Au x Ag 1− x nanoparticles. Chemical Communications, 50(24), pp.3144-3147.

[88] Kawamura, H. and Moritani, K., 1998. Discharge electrolysis in molten chloride: formation of fine silver particles. Plasmas & Ions, 1(1), pp.29-36.

[89] Tokushige, M., Nishikiori, T. and Ito, Y., 2010. Plasma-induced cathodic discharge electrolysis to form various metal/alloy nanoparticles. Russian Journal of Electrochemistry, 46(6), pp.619-626.

[90] Tokushige, M., Tsujimura, H., Nishikiori, T. and Ito, Y., 2013. Formation of metallic Si and SiC nanoparticles from SiO2 particles by plasma-induced cathodic discharge electrolysis in chloride melt. Electrochimica Acta, 100, pp.300-303.

[91] Tokushige, M., Yamanaka, T., Matsuura, A., Nishikiori, T. and Ito, Y., 2009. Synthesis of magnetic nanoparticles (Fe and FePt) by plasma-induced cathodic discharge electrolysis. IEEE transactions on plasma science, 37(7), pp.1156-1160.

[92] Tokushige, M., Hongo, H., Nishikiori, T. and Ito, Y., 2011. Formation of Sm-Co intermetallic compound nanoparticles based on plasma-induced cathodic discharge electrolysis in chloride melt. Journal of the Electrochemical Society, 159(1), p.E5.

[93] Chiang, W.H., Richmonds, C. and Sankaran, R.M., 2010. Continuous-flow, atmospheric-pressure microplasmas: a versatile source for metal nanoparticle synthesis in the gas or liquid phase. Plasma Sources Science and Technology, 19(3), p.034011.

[94] Patel, J., Němcová, L., Maguire, P., Graham, W.G. and Mariotti, D., 2013. Synthesis of surfactant-free electrostatically stabilized gold nanoparticles by plasma-induced liquid chemistry. Nanotechnology, 24(24), p.245604.

[95] Švrček, V., Mariotti, D. and Kondo, M., 2010. Microplasma-induced surface engineering of silicon nanocrystals in colloidal dispersion. Applied Physics Letters, 97(16), p.161502.

[96] Chen, Q., Kaneko, T. and Hatakeyama, R., 2012. Reductants in gold nanoparticle synthesis using gas–liquid interfacial discharge plasmas. Applied Physics Express, 5(8), p.086201.

[97] Chen, Q., Li, J. and Li, Y., 2015. A review of plasma–liquid interactions for nanomaterial synthesis. Journal of Physics D: Applied Physics, 48(42), p.424005.

[98] Riès, D., Dilecce, G., Robert, E., Ambrico, P.F., Dozias, S. and Pouvesle, J.M., 2014. LIF and fast imaging plasma jet characterization relevant for NTP biomedical applications. Journal of Physics D: Applied Physics, 47(27), p.275401.

[99] Kondeti, V.S.K., Gangal, U., Yatom, S. and Bruggeman, P.J., 2017. Ag+ reduction and silver nanoparticle synthesis at the plasma–liquid interface by an RF driven atmospheric pressure plasma jet: Mechanisms and the effect of surfactant. Journal of Vacuum Science & Technology A: Vacuum, Surfaces, and Films, 35(6), p.061302.

[100] Xie, P., Qi, Y., Wang, R., Wu, J. and Li, X., 2019. Aqueous gold nanoparticles generated by ac and pulse-power-driven plasma jet. Nanomaterials, 9(10), p.1488.

[101] Norberg, S.A., Tian, W., Johnsen, E. and Kushner, M.J., 2014. Atmospheric pressure plasma jets interacting with liquid covered tissue: touching and not-touching the liquid. Journal of Physics D: Applied Physics, 47(47), p.475203.

[102] Norberg, S. A., Tian, W., Johnsen, E., & Kushner, M. J. (2014). Atmospheric pressure plasma jets interacting with liquid covered tissue: touching and not-touching the liquid. Journal of Physics D: Applied Physics, 47(47), 475203.

[103] Naidis, G. V. (2014). Production of active species in cold helium–air plasma jets. Plasma Sources Science and Technology, 23(6), 065014.

[104] Bruggeman, P.J., Kushner, M.J., Locke, B.R., Gardeniers, J.G., Graham, W.G., Graves, D.B., Hofman-Caris, R.C.H.M., Maric, D., Reid, J.P., Ceriani, E. and Rivas, D.F., 2016. Plasma–liquid interactions: a review and roadmap. Plasma sources science and technology, 25(5), p.053002.

[105] Wang, Z., Liu, C.J. and Zhang, G., 2009. Size control of carbon black-supported platinum nanoparticles via novel plasma reduction. Catalysis Communications, 10(6), pp.959-962.

[106] Liang, X., Wang, Z.J. and Liu, C.J., 2010. Size-controlled synthesis of colloidal gold nanoparticles at room temperature under the influence of glow discharge. Nanoscale research letters, 5(1), pp.124-129.

[107] Ananth, A. and Mok, Y.S., 2014. Synthesis of RuO2 nanomaterials under dielectric barrier discharge plasma at atmospheric pressure–influence of substrates on the morphology and application. Chemical Engineering Journal, 239, pp.290-298.

[108] Shirai, N., Uchida, S. and Tochikubo, F., 2014. Synthesis of metal nanoparticles by dual plasma electrolysis using atmospheric dc glow discharge in contact with liquid. Japanese Journal of Applied Physics, 53(4), p.046202.

[109] Vanraes, P., Nikiforov, A.Y. and Leys, C., 2016. Electrical discharge in water treatment technology for micropollutant decomposition. Plasma science and technology–progress in physical states and chemical reactions, pp.428-478 (book chapter).

[110] Bruggeman, P., Degroote, J., Vierendeels, J. and Leys, C., 2008. DC-excited discharges in vapour bubbles in capillaries. Plasma Sources Science and Technology, 17(2), p.025008.

[111] Hamdan, A. and Cha, M.S., 2016. The effects of gaseous bubble composition and gap distance on the characteristics of nanosecond discharges in distilled water. Journal of Physics D: Applied Physics, 49(24), p.245203.

[112] Hamdan, A. and Cha, M.S., 2015. Ignition modes of nanosecond discharge with bubbles in distilled water. Journal of Physics D: Applied Physics, 48(40), p.405206.

[113] Shan, Y. and Mostaghimi, J., 2003. Numerical simulation of aerosol droplets desolvation in a radio frequency inductively coupled plasma. Spectrochimica Acta Part B: Atomic Spectroscopy, 58(11), pp.1959-1977.

[114] Dubinov, A.E. and Lyubimtseva, V.A., 2019. Crystallization Features of Aqueous Solutions in Their Droplets Evaporated by Nanosecond Spark Discharge Treatment. High Energy Chemistry, 53(1), pp.1-4.

[115] Dubinov, A.E., Kozhayeva, J.P., Golovanov, V.V. and Selemir, V.D., 2018. Coalescence of liquid droplets under effect of pulsed-periodic spark discharges. IEEE Transactions on Plasma Science, 47(1), pp.76-80.

[116] Woisetschläger, J., Gatterer, K. and Fuchs, E.C., 2010. Experiments in a floating water bridge. Experiments in fluids, 48(1), pp.121-131.

[117] Nomura, S. (2019, October). Fuel Production and Materials Synthesis by In-liquid Plasma. In IOP Conference Series: Materials Science and Engineering (Vol. 619, No. 1, p. 012034). IOP Publishing.

[118] Burakov, V. S., Nevar, E. A., Nedel'Ko, M. I., & Tarasenko, N. V. (2015). Synthesis and modification of molecular nanoparticles in electrical discharge plasma in liquids. Russian Journal of General Chemistry, 85(5), 1222-1237.

[119] Tien, D.C., Chen, L.C., Van Thai, N. and Ashraf, S., 2010. Study of Ag and au nanoparticles synthesized by arc discharge in deionized water. Journal of nanomaterials, 2010.

[120] Chen, L., Mashimo, T., Omurzak, E., Okudera, H., Iwamoto, C. and Yoshiasa, A., 2011. Pure tetragonal ZrO2 nanoparticles synthesized by pulsed plasma in liquid. The Journal of Physical Chemistry C, 115(19), pp.9370-9375.

[121] Hamdan, A., Agati, M. and Boninelli, S., 2021. Selective Synthesis of 2D Mesoporous CuO Agglomerates by Pulsed Spark Discharge in Water. Plasma Chemistry and Plasma Processing, 41(1), pp.433-445.

[122] Gangwar, R.K., Hamdan, A. and Stafford, L., 2017. Nanoparticle synthesis by high-density plasma sustained in liquid organosilicon precursors. Journal of Applied Physics, 122(24), p.243301.

[123] Glad, X., Gorry, J., Cha, M.S. and Hamdan, A., 2021. Synthesis of core–shell copper–graphite submicronic particles and carbon nano-onions by spark discharges in liquid hydrocarbons. Scientific reports, 11(1), pp.1-12.

[124] Park, H., Yoo, S. and Kim, K., 2019. Synthesis of carbon-coated TiO 2 by underwater discharge with capillary carbon electrode. IEEE Transactions on Plasma Science, 47(2), pp.1482-1486.

[125] Hamdan, A., Noel, C., Ghanbaja, J., Migot-Choux, S. and Belmonte, T., 2013. Synthesis of platinum embedded in amorphous carbon by micro-gap discharge in heptane. Materials Chemistry and Physics, 142(1), pp.199-206.

[126] Trad, M., Nominé, A., Noël, C., Ghanbaja, J., Tabbal, M. and Belmonte, T., 2020. Evidence of alloy formation in CoNi nanoparticles synthesized by nanosecond-pulsed discharges in liquid nitrogen. Plasma Processes and Polymers, 17(5), p.1900255.

[127] Hamdan, A. and Cha, M.S., 2016. Low-dielectric layer increases nanosecond electric discharges in distilled water. AIP Advances, 6(10), p.105112.

[128] Hamdan, A. and Diamond, J., 2021. Electrical and optical characterization of a pulsed discharge in immiscible layered liquids: n-heptane and water with various electrical conductivity. Plasma Sources Science and Technology.

[129] Hamdan, A., Abdul Halim, R., Anjum, D. and Cha, M.S., 2017. Synthesis of SiOC: H nanoparticles by electrical discharge in hexamethyldisilazane and water. Plasma Processes and Polymers, 14(12), p.1700089.

[130] Hamdan, A. and Cha, M.S., 2018. Carbon-based nanomaterial synthesis using nanosecond electrical discharges in immiscible layered liquids: n-heptane and water. Journal of Physics D: Applied Physics, 51(24), p.244003.

[131] Krčma, F., Klímová, E., Mazánková, V., Dostál, L., Obradovic, B., Nikiforov, A. and Vanraes, P., 2016. Novel plasma source based on pin-hole discharge configuration. Plasma Medicine, 6(1), pp.21-31.

[132] Descoeudres, A., Hollenstein, C., Demellayer, R. and Wälder, G., 2004. Optical emission spectroscopy of electrical discharge machining plasma. Journal of Physics D: Applied Physics, 37(6), p.875.

[133] Descoeudres, A., Hollenstein, C., Wälder, G. and Perez, R., 2005. Time-resolved imaging and spatially-resolved spectroscopy of electrical discharge machining plasma. Journal of physics D: Applied physics, 38(22), p.4066.

[134] Gigosos, M.A., Gonzalez, M.A. and Cardenoso, V., 2003. Computer simulated Balmer-alpha,-beta and-gamma Stark line profiles for non-equilibrium plasmas diagnostics. Spectrochimica Acta Part B: Atomic Spectroscopy, 58(8), pp.1489-1504.

[135] Landfester, K., Montenegro, R., Scherf, U., Güntner, R., Asawapirom, U., Patil, S., Neher, D. and Kietzke, T., 2002. Semiconducting polymer nanospheres in aqueous dispersion prepared by a miniemulsion process. Advanced Materials, 14(9), pp.651-655.

[136] Kelgenbaeva, Z., Omurzak, E., Takebe, S., Sulaimankulova, S., Abdullaeva, Z., Iwamoto, C. and Mashimo, T., 2014. Synthesis of pure iron nanoparticles at liquid–liquid interface using pulsed plasma. Journal of nanoparticle research, 16(9), pp.1-11.

[137] Li, Q., Weng, S., Wu, J. and Zhou, N., 1998. Comparative study on structure of solubilized water in reversed micelles. 1. FT-IR spectroscopic evidence of water/AOT/n-heptane and water/NaDEHP/n-heptane systems. The Journal of Physical Chemistry B, 102(17), pp.3168-3174.

[138] Zhuang, J., Li, M., Pu, Y., Ragauskas, A.J. and Yoo, C.G., 2020. Observation of potential contaminants in processed biomass using fourier transform infrared spectroscopy. Applied Sciences, 10(12), p.4345.

[139] Coates, J. (2000). Encyclopedia of analytical chemistry. Interpretation of infrared spectra, a practical approach. Wiley, Chichester, 10815-10837.

[140] Zhang, Z.P., Rong, M.Z. and Zhang, M.Q., 2013. Alkoxyamine with reduced homolysis temperature and its application in repeated autonomous self-healing of stiff polymers. Polymer Chemistry, 4(17), pp.4648-4654.

[141] Balan, V., Mihai, C.T., Cojocaru, F.D., Uritu, C.M., Dodi, G., Botezat, D. and Gardikiotis, I., 2019. Vibrational spectroscopy fingerprinting in medicine: from molecular to clinical practice. Materials, 12(18), p.2884.

[142] Hamdan, A., Kabbara, H., Courty, M.A., Cha, M.S., Martinez, J.M. and Belmonte, T., 2017. Synthesis of Carbon–Metal Multi-Strand Nanocomposites by Discharges in Heptane Between Two Metallic Electrodes. Plasma Chemistry and Plasma Processing, 37(4), pp.1069-1090.

[143] Allen, D.T., Palen, E.J., Haimov, M.I., Hering, S.V. and Young, J.R., 1994. Fourier transform infrared spectroscopy of aerosol collected in a low pressure impactor (LPI/FTIR): method development and field calibration. Aerosol Science and Technology, 21(4), pp.325-342.

[144] Bai, Y., Gao, C. and Yin, Y., 2017. Fully alloyed Ag/Au nanorods with tunable surface plasmon resonance and high chemical stability. Nanoscale, 9(39), pp.14875-14880.

[145] Cataldo, F., 2002. An investigation on the optical properties of carbon black, fullerite, and other carbonaceous materials in relation to the spectrum of interstellar extinction of light. Fullerenes, Nanotubes and Carbon Nanostructures, 10(2), pp.155-170.

[146] Hare, J.P., Kroto, H.W. and Taylor, R., 1991. Preparation and UV/visible spectra of fullerenes C60 and C70. Chemical physics letters, 177(4-5), pp.394-398.

[147] Peng, S., Fan, X., Li, S. and Zhang, J., 2013. Green synthesis and characterization of graphite oxide by orthogonal experiment. Journal of the Chilean Chemical Society, 58(4), pp.2213-2217.

[148] Kumar, V., Singh, V., Umrao, S., Parashar, V., Abraham, S., Singh, A.K., Nath, G., Saxena, P.S. and Srivastava, A., 2014. Facile, rapid and upscaled synthesis of green luminescent functional graphene quantum dots for bioimaging. Rsc Advances, 4(40), pp.21101-21107.

[149] Uran, S., Alhani, A. and Silva, C., 2017. Study of ultraviolet-visible light absorbance of exfoliated graphite forms. AIP Advances, 7(3), p.035323.

[150] Chen, R., Nuhfer, N.T., Moussa, L., Morris, H.R. and Whitmore, P.M., 2008. Silver sulfide nanoparticle assembly obtained by reacting an assembled silver nanoparticle template with hydrogen sulfide gas. Nanotechnology, 19(45), p.455604.

[151] Hamdan, A., Gorry, J., Merciris, T. and Margot, J., 2020. Electrical characterization of positive and negative pulsed nanosecond discharges in water coupled with time-resolved light detection. Journal of Applied Physics, 128(3), p.033304.

[152] Tabrizi, N.S., Ullmann, M., Vons, V.A., Lafont, U. and Schmidt-Ott, A., 2009. Generation of nanoparticles by spark discharge. Journal of Nanoparticle Research, 11(2), pp.315-332.

[153] Saito, G. and Akiyama, T., 2015. Nanomaterial synthesis using plasma generation in liquid. Journal of Nanomaterials, 2015.

[154] Yang, C.A.O., Guangzhou, Q.U., Tengfei, L.I., Jiang, N. and Tiecheng, W.A.N.G., 2018. Review on reactive species in water treatment using electrical discharge plasma: formation, measurement, mechanisms and mass transfer. Plasma Science and Technology, 20(10), p.103001.

[155] Judée, F., Simon, S., Bailly, C. and Dufour, T., 2018. Plasma-activation of tap water using DBD for agronomy applications: Identification and quantification of long lifetime chemical species and production/consumption mechanisms. Water research, 133, pp.47-59.

Annexes